RESEARCH



Pharmacokinetic modeling of solid and hollow gold-coated superparamagnetic iron oxide nanoparticles for brain-targeted therapeutics: prediction and experiment

Hanwen Hu¹ · Muzhaozi Yuan¹ · Jingfan Chen¹ · Tianzhu Fan¹ · Nguyen Nguyen¹ · Caitlin A. Madison² · Tianhao Yan³ · Zhifeng Xiao³ · Ying Li¹ · Shoshana Eitan² · Hong-cai Zhou³ · Jean Phillippe Pellois³ · Ya Wang^{1,4,5}

Received: 1 October 2023 / Revised: 25 January 2024 / Accepted: 2 April 2024 / Published online: 22 April 2024 © The Author(s), under exclusive licence to Springer Nature Switzerland AG 2024

Abstract

Magneto-plasmonic nanoparticles (MPNPs), such as solid gold (Au) or hollow gold (HG) coated superparamagnetic iron oxide (SPIO) nanoparticles (NPs), have attracted increasing attention for brain-targeted therapeutics. This is due to their supreme magnetic targeting capability, light-to-heat conversion efficiency, and biocompatibility. Though promising, their therapeutic efficiency is difficult to predict because of the complex absorption, distribution, metabolism, and excretion process and the intrinsic and extrinsic properties of the blood–brain barrier (BBB). This paper presents a modern physiologically based pharmacokinetic (PBPK) model to predict pharmacokinetic (PK) behaviors of brain-targeting MPNPs and investigate their morphology and surface function-dependent BBB crossing efficiency. This model quantifies intrinsic and extrinsic properties of PK parameters, including phagocytic cellular uptake rate and brain permeability. This model successfully predicts the biodistribution of functionalized Au-SPIO (18.42±0.23 nm) and HG-SPIO (73.65±1.46 nm) MPNPs in 8-week-old adult mice in a 16-h window after intraperitoneal (IP) injection. These predictions agree well with the experimental data with a low absolute average fold error (1.5381 for Au-SPIO and 1.1225 for HG-SPIO NPs). Interestingly, Au-SPIO MPNPs with thinner plasmonic layers result in higher magnetization levels and thus lead to more efficient BBB crossing. Static magnetic field stimulation could improve brain accumulation of IP-injected Au-SPIO and HG-SPIO NPs by up to 4.9% and 1.4%, respectively. Additionally, IP injection led to higher brain accumulation compared to intravenous injection. This modern PBPK model can guide MPNP design optimization for brain-specific therapeutics.

 $\textbf{Keywords} \ \ Modern \ pharmacokinetic \ modeling \cdot Brain-targeted \ the rapeutics \cdot Au-SPIO \cdot HG-SPIO \cdot Magnetic \ field \cdot In \ vivo \ biodistribution$

1 Introduction

Compared to non-plasmonic nanoparticles (NPs), plasmonic NPs, typically made from metals like gold or silver, exhibit distinctive optical characteristics due to their conduction

Hanwen Hu, Muzhaozi Yuan and Jingfan Chen are co-first author.

Tianzhu Fan, Nguyen Nguyen and Caitlin A. Madison are co-second author.

- Muzhaozi Yuan
 Muzhaozi.yuan@tamu.edu
- ✓ Ya Wang ya.wang@tamu.edu
- J. Mike Walker '66 Department of Mechanical Engineering, Texas A&M University, College Station, TX 77843, USA
- Department of Psychological and Brain Sciences, Texas A&M University, College Station, TX 77843, USA

electrons interacting with light [1]. This interaction is governed by plasmon resonance, which occurs when light's frequency aligns with the natural oscillation frequency of the metal's surface electrons against the positive nuclei's restoring force. When these nanoparticles are exposed to light, the free electrons on the metal's surface vibrate together, generating potent electric fields. This phenomenon amplifies optical behaviors such as scattering and absorption. As a result,

- Department of Chemistry, Texas A&M University, College Station, TX 77843, USA
- Department of Electrical and Computer Engineering, Texas A&M University, College Station, TX 77843, USA
- Department of Biomedical Engineering, Texas A&M University, College Station, TX 77843, USA



plasmonic nanoparticles are highly valuable in applications like sensing and photothermal therapy [2]. In addition to plasmonic properties, magneto-plasmonic nanoparticles (MPNPs) have drawn increasing attention for brain-targeted therapeutics due to their unique properties of magnetic targeting [3], magnetic [4], and plasmonic [5] hyperthermia, excellent biocompatibility [6], and drug loading capacity [7]. We recently developed solid gold (Au)-coated superparamagnetic iron oxide (SPIO) MPNPs with a high photothermal conversion efficiency [8, 9], enhanced neurodegeneration [9, 10], and magnetic-field promoted cellular uptake [11]. They exhibit more substantial magneto-plasmonic properties than other compounds [12–14], but their limited tissue penetration depth has restricted their brain-targeting therapeutic efficiency [15]. In contrast, a hollow gold (HG) MPNP with multiple SPIO cores enclosed [16] and a thin gold outer layer offers a promising solution to overcome this limitation by penetrating deeper into brain tissues. This is achieved by fine-tuning their surface plasmon resonance (SPR) to near-infrared (NIR) regions by varying the thickness of the gold shells.

However, designing MPNPs with optimal nanostructure and surface functions facilitating brain-targeting therapeutics is still a persistent challenge. This is mainly because it is difficult to predict the complex absorption, distribution, metabolism, and excretion (ADME) process and the blood-brain barrier (BBB) crossing behaviors of MPNPs [17]. Traditional physiologically based pharmacokinetic (PBPK) models can predict the time history of the ADME process of MPNPs within major organs, but the brain due to low brain permeabilities and lack of understanding of intrinsic and extrinsic parameters related to BBB crossing. Notably, evaluating the penetration ability of MPNPs across the BBB is crucial in brain-targeting therapeutics [18]. This paper presents a modern PBPK model that can predict pharmacokinetic (PK) behaviors of brain-targeting MPNPs and investigate their morphology and surface function-dependent BBB crossing efficiency. This current PBPK model quantifies intrinsic and extrinsic properties of PK parameters, including phagocytic cellular uptake rate and brain permeability. Some PK parameters, historically challenging to collect, are curve-fitted using in vivo data collected from major organs of mice and rats.

Traditional PBPK models are either diffusion-limited (also called permeability-limited model) or perfusion-limited based. The former model works better for MPNPs larger than 50 nm [19], where the permeability of the cell membrane limits the distribution of the substance into the tissue, as the tissue's tight junctions and transporters create a barrier and limit the rate of drug or chemical exchange between blood and tissues. The latter model assumes that the transport of compounds across the blood tissue barriers is the rate-limiting step of biodistribution [20]. That is, the

rate of drug entering the compartment (tissue) is determined by the organ's blood flow rate, where the compound distributes freely across the membranes without diffusion barriers or significant transporter contributions [21]. For a diffusion-limited model, the equilibrium of vascular versus extravascular space cannot be obtained instantly. While the perfusion-limited model considers blood perfusion as the main limitation for MPNP penetration, the transportation between blood and tissue reaches equilibrium immediately [21]. The diffusion-limited model is usually more appropriate for predicting the in vivo biodistribution of MPNPs since it takes a long time to cross the cell membrane [22]. However, neither traditional model considers enough parameters to predict BBB crossing efficiency accurately. For example, a diffusion-limited PBPK model was created to predict brain accumulation of spherical polyethylene glycol (PEG)-coated Au nanoparticles (NPs) (13 nm and 100 nm in diameter). However, their average fold error is 2 and 3 [23]. The main reason is that their parameters are mainly obtained from different animal models in the literature, such as rats and mice, dogs, and pigs, and they did not consider the size impacts on phagocytic (PC) cellular uptake rate, plasma distribution coefficient, and many other parameters.

A perfusion model was created to predict tissue accumulation of Au NPs (16 nm in diameter) in mice and their interspecies extrapolation from mice to rats using the organism-specific (excretion and PC cellular uptake) parameters of rats from the literature to validate their model [24]. This model does not consider the impact of size and tissue permeability on the PBPK model. A recent study also discussed the effect of different administration routes, including intravenous (IV), oral, instillation, and inhalation of spherical Au NPs (18 nm in diameter) [25]. It concluded that the surface area determines the cellular uptake rate regardless of the administration route. However, their model does not quantify the impact of NP size on the PBPK parameters. Others intend to predict the in vivo biodistribution of PEGcoated Au NPs (13 nm in diameter) in the corresponding organ tissue shield using a perfusion-limited PBPK model fitted with in vitro data of human lung bronchial epithelial cell lines [26]. However, the cell line model does not consider macrophage-mediated uptake. In vitro results may lead to overestimating NP burden for organs like the brain with natural barriers compared with in vivo data. Recently, more efforts have been made to utilize the in vitro results to parametrize the PBPK models to increase their prediction accuracy. Our previous PBPK model integrated in vivo data to predict the biodistribution of Au-SPIO NPs (17.50 nm in diameter) in adult mice under static and dynamic magnetic fields (MF) [17]. Significantly, this model formulated traditionally neglected brain permeabilities of Au-SPIO NPs using in vivo data [17].



To better predict brain accumulation of generalized MPNPs with different morphologies. This paper presents a modern PBPK model to study intrinsic and extrinsic parameters associated with tissue uptake and brain targeting efficiency. Using comprehensive quantification of PK parameters using in vivo data, this modern PBPK model can predict a history (16-h) brain accumulation of Au-SPIO and HG-SPIO NPs in 8-week-old adult mice after intraperitoneal (IP) and IV injection. This model presents the MPNP parametric dependence on brain permeability, crossing, and brain-targeting efficiency, unlike commercial software, such as Simcyp Simulator, PBPKPlus, and PopPKPD, which do not provide many options for fine-tuning PBPK parameters such as brain permeability, distribution coefficients, and PC uptake rate. These are critical for designing brain-targeting MPNPs with maximal efficiency. In addition, our model considers the parametric importance of magnetic field stimulation intrinsic and extrinsic properties of PK parameters to better design MPNPs with optimal nanostructure and surface properties. We also compared the in vivo results of IP and IV-injected MPNPs. The local sensitive analysis (LSA) and parameter optimization provide comprehensive guidance for designing MPNPs with higher brain accumulation.

Section 2 describes the synthesis and functionalization of these two types of MPNPs (Au-SPIO and HG-SPIO NPs) used for modeling and in vivo validation. Section 3 presents the development of the PBPK model and identifies each essential parameter. Finally, Sect. 4 compares the predicted results and the measured in vivo data in adult mice to assess the model's accuracy. We also presented N2A cell viability to verify the non-toxic properties of the two types of MPNPs injected. A local LSA ranks the importance of parameters affecting MPNP concentration in blood and the brain. Parameters are optimized using the Symbiology-optimized toolbox to improve prediction accuracy. The final section discusses factors affecting the BBB crossing, including outer diameters of MPNPs, external MF applied, and injection methods.

2 Material and methods

This section discusses synthesizing and characterizing two types of MPNPs.¹ They are functionalized with PEG and insulin to increase the blood half-life and the BBB crossing efficiency, respectively [].

2.1 Materials

SPIO NPs (EMG304) were obtained from Ferrotec (Livermore, CA). All other NP synthesis and functionalization

reagents are obtained from Sigma-Aldrich (St. Louis, MO). DMEM (Dulbecco's Modified Eagle Medium) contains essential nutrients, vitamins, amino acids, and glucose to support cell growth and is widely used for in vitro cultivation. PBS (phosphate-buffered saline) is a buffer for cell washing and diluting substances. Trypsin EDTA is an enzyme used in cell culture to dissociate adherent cells from the surface of a culture dish. SYTO 59 and SYTOX Green are fluorescent nucleic acid stains that selectively stain dead and alive cells for cell viability experiments. These substances are obtained from Thermo Fisher Scientific (Harris County, TX, USA).

2.2 Synthesis of Au-SPIO core-shell structure

We synthesized the Au-SPIO NPs according to our previous protocol [6]. In summary, 2 mL of 4.66-mM SPIO solution was stirred with 6 mL of 0.1 M sodium citrate for 10 min to exchange the absorbed OH – with citrate anions. The mixture was then diluted to 100 mL with DI water. A total of 0.5 mL of 1% HAuCl₄ solution was added to the mixture. The pH was adjusted to 9–10 using 0.1 M NaOH solution. Then, 0.6 mL of 0.2-M hydroxylamine hydrochloride was added to the mixture to form the Au coating. The color of the mixture changed from brown to purple in several minutes. After that, another 0.5 mL of 1% HAuCl₄ was added to the solution, followed by 0.2 mL of 0.2 M hydroxylamine hydrochloride. This process was repeated several times to form a thicker Au coating. The color of the final solution changed from purple to red.

2.3 Synthesis of HG-SPIO core-shell structure

At first, the SPIO core NPs were synthesized by a simple co-precipitation method. First, 2 mmol of FeCl₃, 1 mmol of FeSO₄, and 0.1 mmol of sodium dodecyl sulfate (SDS) were dissolved in 200 mL of deionized (DI) water. Then 80 mL of 125-mM NaOH solution was slowly added at room temperature. Once the mixed solution appeared black, it was centrifuged and washed with DI water and ethanol several times. Then, the precipitate (Fe₃O₄) was collected by a magnet and reserved in 80 mL of DI water (Fe₃O₄ suspension) in a refrigerator. To further oxidize Fe_3O_4 to magnetic γ - Fe_2O_3 , 20 mL of Fe₃O₄ suspension was diluted to 100 mL with DI water and then added with 0.1 mL of concentrated HNO₃ (70%). The mixed solution was heated under 90 °C in an oil bath for 30 min, and its appearance changed from black to brown during the procedure, indicating the oxidation of Fe_3O_4 to γ - Fe_2O_3 . Finally, the solution was centrifuged and washed with DI water, and the precipitate $(\gamma - Fe_2O_3)$ was collected and preserved in 20 mL of DI water (SPIO suspension). Secondly, Ag-SPIO NPs were fabricated as templates. To do this, 0.5 mL of SPIO suspension and 1 mL of 30-mM



¹ In this manuscript, all MPNPs are functionalized with PEG and insulin to promote blood half-life and brain permeability unless otherwise specified.

trisodium citrate were added to 17 mL of DI water. The mixed solution was heated uniformly under 60 °C in the oil bath for 10 min, then 2 mL of 20 mM AgNO₃ was slowly added into the solution. After 10 min, 5 mL of 5 mM NaOH was slowly added to the solution. After another 30 min, 0.5 mL of 0.5-M hydroxylamine hydrochloride was added into the solution to facilitate the precipitation process of Ag⁺ on the surface of γ-Fe₂O₃. The heating process continued for 210 min, and finally, the product's appearance became brownish yellow, indicating the formation of an Ag-SPIO suspension. Finally, for fabricating HG-SPIO NPs, 0.53 mL of 25 mM HAuCl₄ was slowly added into the Ag-SPIO suspension under 60 °C when the Ag⁺ on the surface of γ-Fe₂O₃ began to be replaced by Au³⁺. The heating process for this displacement reaction continued for another 30 min, and then the product in blue color was collected, which was marked as HG-SPIO suspension.

2.4 Functionalization of Au-SPIO and HG-SPIO NPs using PEG and insulin

The prepared Au-SPIO and HG-SPIO NPs were functionalized by PEG first. Two types of PEG solutions were applied, including 5 mg mL⁻¹ mPEG-SH (molecular weight (MW), 5000 Da) and 5 mg mL^{-1} SH-PEG-COOH (MW, 3400 Da). The Au-SPIO and HG-SPIO NPs' suspensions were thoroughly mixed with a hybrid PEG solution (including 15% of SH-PEG-COOH and 85% of mPEG-SH) by a ratio of 45 µL of PEG solution at the concentration of 5 mg/mL per mg of Au-SPIO NPs and HG-SPIO NPs, respectively. Then, the resulting PEG functionalized Au-SPIO NPs and HG-SPIO solutions were stored in a refrigerator for 24 h. Then, for the insulin conjugation with Au-SPIO-PEG NPs, 2 mM of 1-Ethyl-3-(3-dimethyl aminopropyl) carbodiimide hydrochloric acid (HCl) (EDC, 22980-Sigma-Aldrich, St. Louis, MO, USA) and 5 mM of N-hydroxysulfosuccinimide sodium salt (NHS, 24500-Sigma-Aldrich, St. Louis, MO, USA) were added directly to 1 mL of insulin (11061-Sigma-Aldrich, St. Louis, MO, USA) at the concentration of 10 mg/mL. The solution was mixed well and reacted for 15 min at room temperature. A total of 0.02 mL of the resulting mixture was added directly to 12 mL of 1 mg/mL Au-SPIO-PEG NPs. The solution was left to stir overnight to ensure the conjugation of the PEG layer to the insulin. Au-SPIO-PEG-insulin NPs were purified after the solution was centrifuged. The final concentration was 3 mg/mL, denoted as functionalized Au-SPIO NPs. For the insulin conjugation with HG-SPIO-PEG NPs, 1 mL of 1 mg mL⁻¹ insulin was thoroughly mixed with 2 mL of 5 mM EDC solution and 2 mL of 5 mM NHS solution. Then, 1 mL of the resulting mixture was added to 12 mL of 1 mg mL⁻¹ HG-SPIO-PEG suspension, and the mixture was left overnight to ensure the conjugation of the PEG layer to the insulin. Finally, the prepared HG-SPIO-PEG-insulin NPs were collected by centrifugation at 12,000 rpm for 15 min and washed twice to remove the uncoated insulin. The resultant was denoted as functionalized HG-SPIO NPs. The MPNPs used for the following in vivo experiments are fully functionalized Au-SPIO and functionalized HG-SPIO NPs.

2.5 Characterization of functionalized Au-SPIO and HG-SPIO NPs

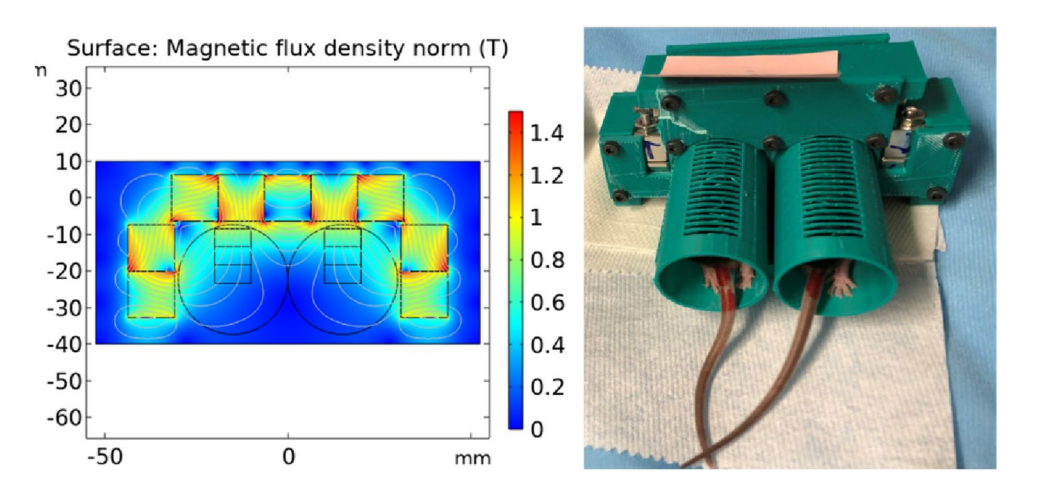
We use the transmission electron microscope (TEM) to assess the morphological characteristics and determine the MPNP size distribution. In addition, the detailed structure and morphology of the HG-SPIO NPs were analyzed on an FEI Tecnai G2 F20 ST field emission transmission electron microscope (FE-TEM), operated at an accelerating voltage of 200 kV. The size distribution of the MPNPs was analyzed by measuring a minimum of 100 NPs. The inner and outer diameters of each NP were measured using ImageJ. Their light absorption spectra were measured using a Hitachi U-4100 UV-Vis-NIR spectrophotometer (500–1200 nm). In a typical measurement, 3 ml of NP solution was added to the cuvette. The hydrodynamic diameters and zeta potential of MPNPs, with and without functionalization, were measured by dynamic light scattering (DLS) on a Zetasizer apparatus (Malvern Instruments; Malvern, UK). The hydrodynamic diameter was calculated from the intensity-weighted distribution function obtained by CONTIN analysis of the correlation function embedded in Malvern software. All measurements were performed in triplicates.

2.6 Cell viability evaluation

Neuro2A cells are known for their neuron-like characteristic and commonly serve as a versatile in vitro model for many investigations in neuronal functions, neurotoxicity, and responses to stimuli [27]. Thus, we use N2A cells to evaluate the toxicity of Au-SPIO and HGNS-SPIO to neuronal cells. N2A cells were seeded into a 48-well plate and cultured for 1 day. The cells were then incubated with Au-SPIO and HG-SPIO NPs at different concentrations for 1, 3, and 5 days. After each incubation period, the cells were harvested by detaching them with 0.25% trypsin-EDTA and neutralizing them in the Dulbecco's Modified Eagle Medium (DMEM). The cell suspension was then centrifuged, and the supernatant was discarded. The cells were stained with SYTOX Green and SYTO 59 Red for flow cytometric analysis. The staining solutions were diluted at 1:2000 for SYTOX Green and 1:1000 for SYTO 59 Red for 30 min in the dark. Cell viability was measured using a BD Accuri C6 flow cytometer equipped with FL 1 detector (553 nm) and FL 4 detector (675 nm); event number > 10,000.



Fig. 1 a The magnetic flux simulation (front view) of the magnetic applicator containing a linear Halbach array and b the magnetic applicator hosting two mice



2.7 Cell uptake rate measurement

The cell uptake rate for Au-SPIO and HG-SPIO NPs was measured using elemental analysis. N2A cells were cultured in a 48-well plate for 1 day and then incubated with Au-SPIO and HG-SPIO NPs at 40 ug/ml concentrations. After 2, 4, 8, and 12 h of incubation, the cells were washed three times with PBS to remove unassociated and unattached NPs. The cells were then harvested by detaching them with 0.25% trypsin-EDTA and neutralizing them in DMEM before transferring them to microcentrifuge tubes. The cells were then centrifuged to remove the top solutions containing free NPs not taken up by the cells. The remaining cells were digested using aqua regia, and the amount of gold was quantified using a PerkinElmer NexION 300D Inductively Coupled Plasma Mass Spectrometer (ICP-MS).

2.8 In vivo biodistribution of Au-SPIO and HG-SPIO NPs in adult mice

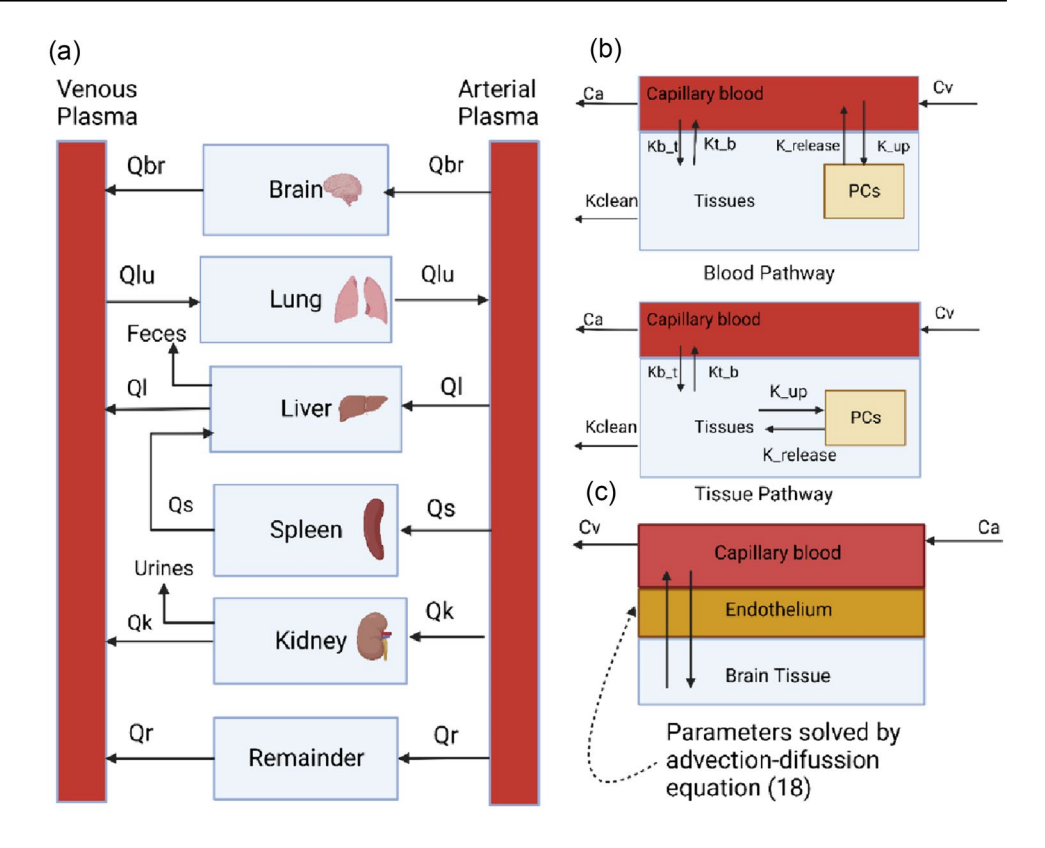
We used 8-week-old male C57BL/6N mice (Envigo Lab, Indianapolis, IN, USA). We housed them in a temperature-controlled (21 ± 2 °C, humidity 45%) vivarium with a 12-h light/12-h dark cycle (lights on at 07:30). We use male mice in our study to maintain consistency for direct comparability with existing literature [28–30] and to build upon established knowledge. To study the effect of MFs, injection methods, and MPNP types, mice were injected (Au-SPIO-PEG-insulin or HG-SPIO-PEG-insulin NPs) at 30 mg/kg and were randomly divided into eight treatment groups as follows: (a) MF-, IV, functionalized Au-SPIO NPs; (b) MF+, IV, functionalized Au-SPIO NPs; (c) MF – , IP, functionalized Au-SPIO NPs; (d) MF + , IP, functionalized Au-SPIO NPs; (e) MF – , IV, functionalized HG-SPIO NPs; (f) MF+, IV, functionalized HG-SPIO NPs, (g) MF -, IP, functionalized HG-SPIO NPs; and (h) MF+, IP, functionalized HG-SPIO NPs (number of animals = 3 for each experimental group). The mice in the corresponding groups were subjected to MF for 30 min and were anesthetized right before the MF treatment.

The mice were anesthetized and sacrificed at 2, 4, 8, and 12 h post-injection. The injected dose of 30 mg/kg, of which gold is about 77.4% for Au-SPIO and 58.9% for HG-SPIO NPs, is considered safe for mice and for detecting gold concentration in the brain. According to the literature, Au NPs were IV injected into mice with a dose as high as 1000 mg/ kg. The dose was well-tolerated, and no adverse effects were observed 24 h after injection [31]. It is also reported that gold NPs with insulin coating at 273 mg/kg were IV injected into mice [32]. Our dose was within the range reported in the literature. At the designated post-injection time, the brain (dissected into midbrain, cortex, and cerebellum), liver, lung, and blood samples were collected and frozen immediately at – 80 °C. All procedures were conducted by the National Institutes of Health Guide for the Care and Use of Laboratory Animals and were approved by the Institutional Animal Care and Use Committee. As shown in Fig. 1a-b, we built an MF applicator using a linear Halbach array composed of 9 magnets for treating two mice simultaneously (NdFeB, grade N52, the core strength of 1.48 T, dimensions $12.7 \times 12.7 \times 12.7$ mm, K&J Magnetics, Inc.). The array was specialized for a mouse's head as a ring with a 38 mm inner diameter (approximately the size of the diameter of the mouse head), 78 mm outer length, and 16 mm thick.

We performed statistical analysis using the Mann–Whitney *U*-test to estimate whether there is a significant difference between the two treatment groups of Au accumulation. We consider a p-value < 0.05 as a significant difference. We express all the results using the average and the standard error of the mean based on at least three independent experiments.



Fig. 2 a The permeability-limited PBPK model considering brain permeability. Q and C are blood flow and NP concentration. b Different sub-compartment representations of organs in the PBPK model: blood and PC transport for Au-SPIO NPs and tissue and PC transport for HG-SPIO NPs. c The brain permeability was obtained from advection—diffusion equations



3 PBPK Modeling

3.1 PK properties of MPNPs

The developed PBPK model considers diffusion from blood to major compartments, including the brain, lungs, liver, spleen, kidneys, and the rest of the mouse body, as shown in Fig. 2a. Each compartment comprises three sub-compartments representing capillary blood, tissue, and PCs. We consider two diffusion pathways: Au-SPIO NPs transport blood and PCs. while HG-SPIO NPs transport between tissue and PCs, as illustrated in Fig. 2b. We model the brain permeability using an advection-diffusion equation, as shown in Fig. 2c. Empirical studies suggest a 60–80% absorption rate. Examples include $64.8 \pm 11.9\%$ for IP-injected SPIO NPs in mice (18–20 nm, 25 mg/kg) [33], 69% for IP-injected docetaxel (20 nm, 8 mg/ kg) [34], and 76% for Au NPs (20 nm 10 mg/kg) [24]. Based on this evidence and microscope observations, we assume that 76% of functionalized MPNPs entered blood circulation after IP injection. Subsequently, they passed through the capillary membrane of each organ via different endocytic pathways, described by the diffusion-limited model. We assume their excretion rates by the liver and kidneys are constant. Therefore, ordinary differential equations can mathematically describe their concentrations at each compartment and sub-compartment. Works of the literature suggest that MPNP of different sizes are taken up via different pathways: the tissue and blood pathway for smaller (20 nm) [35] and larger (50 nm) NPs [36], respectively.

Thus, we describe the kinetics of Au-SPIO (18.42 ± 0.23 nm) and HG-SPIO NPs (73.65 ± 1.46 nm) in the PCs, capillary blood, and tissue of each organ:

For Au-SPIO NPs:

$$R_{\text{blood}_{t}} = Q_{t} \times (C_{a} - \text{CV}_{t}) - \text{PA}_{t} \times \text{CV}_{t} + \frac{\text{PA}_{t} \times \text{C}_{\text{tissue}_{t}}}{P_{t}}$$

$$+ K_{\text{up}_{t}} \times A_{\text{b}_{t}} - K_{\text{release}_{t}} \times A_{\text{pc}_{t}}$$

$$(1)$$

For HG-SPIO NPs:

$$R_{blood_t} = Q_t \times (C_a - CV_t) - PA_t \times CV_t + \frac{PA_t \times C_{tissue_t}}{P_t}$$
(2)

Here, subscript t represents the organ t, R_{blood_t} is the rate of changes in the mass of the MPNPs in the capillary of the organ t, Q_t (L/h) is the blood flow to the organ, C_a (mg/l) and CV_t (mg/L) are the MPNP concentrations in the arterial and venous blood, respectively, PA_t (L/h) is the permeability area cross product between the capillary blood and the tissue (the product of permeability coefficient between capillary blood and tissue PAC_t (unitless) and regional blood flow Q_t (L/h)), C_{tissue_t} (mg/L, μ g/g or ng/g) is the MPNP concentration in the tissue, P_t (unitless) is the tissue/plasma distribution coefficient. K_{up_t} (1/h) and $K_{release_t}$ (1/h) are the PC uptake and release rate (constant), respectively, and A_{b_t} (mg) and A_{pc_t} (mg) are the mass of the MPNPs in the capillary blood and the PCs, respectively.



Table 1 PB parameters used in our PBPK model

Parameter		Symbol	Mean value
Body weight (kg)		BW	0.025
Cardiac output (L/h/kg ^{0.75})		QCC	16.5
	Blood flow to each compartment (L/h)		
Liver		$Q_{ m L}$	0.167
Spleen		$Q_{ m s}$	0.011
Kidneys		$Q_{ m k}$	0.094
Lungs		$Q_{ m Lu}$	1.037
Brain		$Q_{ m BR}$	0.034
Remainder		$Q_{ m RE}$	0.730
	Mass of the tissue in each compartment (kg)		
Liver		$V_{ m t_L}$	$9.49*10^{-4}$
Spleen		$V_{\mathrm{t_S}}$	$1.04*10^{-4}$
Kidneys		$V_{ m t_K}$	$3.23*10^{-4}$
Lungs		$V_{ m t_Lu}$	$8.75*10^{-5}$
Brain		$V_{ m t_BR}$	$4.12*10^{-4}$
Remainder		$V_{ m t_RE}^-$	$2.04*10^{-2}$
	Mass of the blood (kg)		
Venous blood		V_{V}	$9.80*10^{-4}$
Arterial blood		$V_{ m a}$	$2.45*10^{-4}$
	Mass of the capillary blood in each compartment (kg)		
Liver		$V_{ m b_L}$	$4.26*10^{-4}$
Spleen		$V_{ m b_S}$	$2.13*10^{-5}$
Kidneys		$V_{ m b_K}$	$1.02*10^{-4}$
Lungs		$V_{ m b_Lu}$	$8.75*10^{-5}$
Brain		$V_{ m b_BR}^-$	$1.28*10^{-5}$
Remainder		$V_{ m b_RE}^-$	$8.50*10^{-4}$

For Au-SPIO NPs:

$$R_{tissue_t} = PA_t \times CV_t - \frac{PA_t \times C_{tissue_t}}{P_t},$$
(3)

For HG-SPIO NPs:

$$R_{tissue_{t}} = PA_{t} \times CV_{t} - \frac{PA_{t} \times C_{tissue_{t}}}{P_{t}} + K_{up_{t}} \times A_{b_{t}} - K_{release_{t}} \times A_{pc_{t}}$$
(4)

Here, $R_{\rm tissue_t}$ (mg/h) is the rate of changes in the mass of the MPNPs in the tissue. Given the average weight of the 80 mice of 0.025 kg, we calculated the PB parameters, including blood flow to different compartments ($Q_{\rm t}$), the compartment mass ($V_{\rm b_t}$ and $V_{\rm t_t}$), and the blood mass ($V_{\rm v}$ and $V_{\rm a}$), as listed in Table 1. The average percentage of blood flow to the compartments and the percentage of compartment volumes (capillary blood and tissue) to the body weight were adopted from the literature [37].

Besides these PB parameters in Table 1, which are only affected by animal type, other PK parameters are essential to simulate the PBPK of MPNPs, as listed in Table 2. As

discussed in the next section, those parameters are highly affected by the MPNP's properties.

3.2 Estimation of permeability

3.2.1 Brain permeability based on the indicator diffusion method

The permeability for the brain tissue is usually assumed to be zero in most reported PBPK models because of the low BBB crossing ability for some NPs and drugs [36]. It is not accurate enough to simulate the MPs accumulation in the brain. Our model assumes that the brain permeability is not negligible and discusses the effect of the applied magnetic field's enhancement on the MPNP's BBB crossing efficiency by the advection—diffusion method. To estimate the permeability coefficient in the brain, we consider the entry of MPNPs through the Circle of Willis (CoW), an arterial junction supplying blood to the brain. It details the arterial structure of the brain, including the internal carotid arteries (ICAs), vertebral arteries (VAs), anterior cerebral



Table 2 MPNP-related parameters used for simulating their transportation in the brain

Parameter	Symbol	Value
Diameter of Au-SPIO NPs	$d_{ m Au}$	18.42 nm (±0.23)
Hydrodynamic diameter Au-SPIO NPs	$d_{ m HAu}$	$38.4 \text{ nm} (\pm 1.21)$
Outer diameter of HG-SPIO NPs	$d_{ m HG}$	$73.65 \text{ nm} (\pm 1.21)$
Hydrodynamic diameter of HG-SPIO NPs ^a	$d_{ m HHG}$	$125.8 \text{ nm} (\pm 0.60)$
SPIO density ^a	$ ho_{ m spio}$	5240 kg/m^3
Au density ^a	$ ho_{ m Au}$	$19,320 \text{ kg/m}^3$
Initial concentration of Au-SPIO NPs ^a	$C_{ m in}$	1 mol/m ³
Magnetic gradient ^b	$\nabla(\left \overrightarrow{H}\right ^2)$	$1.46*10^{13}A^2/m^3$
ICA inflow rate ^c	$Q_{ m ICA}$	0.012 L/h
VA inflow rate ^c	$Q_{ m va}$	0.004 L/h
Blood viscosity ^c	η	0.003 Pa.s
Temperature ^c	T	310 °K (body temperature)
Brownian diffusion coefficient ^d	$D_{ m B}$	$7.27*10^{-12} \text{ m}^2/\text{s}$
Blood cells diffusion coefficient ^d	$D_{ m S}$	$3.92*10^{-10} \text{ m}^2/\text{s}$
Total diffusion coefficient in blood ^d	$D_{ m total}$	$3.99*10^{-10} \text{ m}^2/\text{s}$
Diffusion coefficient (in membrane) ^d	$D_{ m endo}$	$1.15*10^{-12} \text{ m}^2/\text{s}$
Diffusion coefficient (in tissue) d	$D_{ m tissue}$	$2.23*10^{-10} \text{ m}^2/\text{s}$

^aValues obtained from the NPs characterization discussed in Sect. 4.1

arteries (ACA), middle cerebral arteries (MCA), basilar artery (BA), and posterior cerebral arteries (PCA). According to statistical analysis, the blood inflow distribution is ICA (36% each) and VA (14% each), and the total brain blood flow is 0.034 L/h. We confirmed these rates align with existing literature [38].

Brownian motion must be considered when the energy exerted by the applied force in moving the particle at a distance equal to its diameter is less than or comparable to thermal energy. To understand the random movement of our MPNPs, we first calculate the Brownian diffusion D_R :

$$D_{\rm B} = \frac{K_b^* T}{3\pi \eta D_{\rm H}} \tag{5}$$

Here T is the absolute temperature (measured in Kelvin) and K_B is Boltzmann's constant. η is the dynamic blood viscosity Pa.s) and D_H is the particle hydrodynamic diameter (nm). Another diffusive mechanism that influences the MPNP motion in vessels is shear-induced diffusion. As blood is a highly concentrated fluid with red blood cells (RBCs) suspended in plasma where sheared cell–cell collisions give rise to random motions with a diffusive character, the shear-induced diffusion coefficient, D_S can be modeled as

$$D_{S} = K_{S}(r_{b})^{2} \gamma \tag{6}$$

Here $K_S \approx 5 \times 10^{-2}$ is a dimensionless coefficient dependent on RBCs concentration, r_b is the radius of RBCs (μ m) and $\dot{\gamma} = 4 \times \frac{V_{\rm Bmax}}{d_{\rm B}}$ is the local value of the fluid shear rate. $V_{\rm Bmax}$ (μ m/s) and d_B (μ m) are the maximum centerline velocity and blood vessel diameter, respectively. Thus, the total diffusion coefficient in the blood is:

$$D_{\text{total}} = D_{\text{B}} + D_{\text{S}} \tag{7}$$

An empirical equation calculates the diffusion coefficient in the endothelial layer [39]:

$$D_{\text{endo}} = D_{\text{B}} \left(1 - \frac{d}{d_{\text{pore}}} \right)^{2} (1 - 2.1 \left(\frac{d}{d_{\text{pore}}} \right) + 2.09 \left(\frac{d}{d_{\text{pore}}} \right)^{3} - 0.95 \left(\frac{d}{d_{\text{pore}}} \right)^{5}$$
(8)

where d (nm) is the average diameter of MPNPs and $d_{pore} \approx 20 nm$ is the average diameter of the pores in a membrane, [39] where the diffusion coefficient in the tissue is defined as:

$$D_{\text{tissue}} = 0.56D_{\text{B}} \tag{9}$$

The magnetization of MPNPs can be expressed as [40]:

$$m_p = V_p \frac{3(\chi_p - \chi_f)}{((\chi_p - \chi_f) + 3(\chi_f + 1))} H_a$$
 (10)

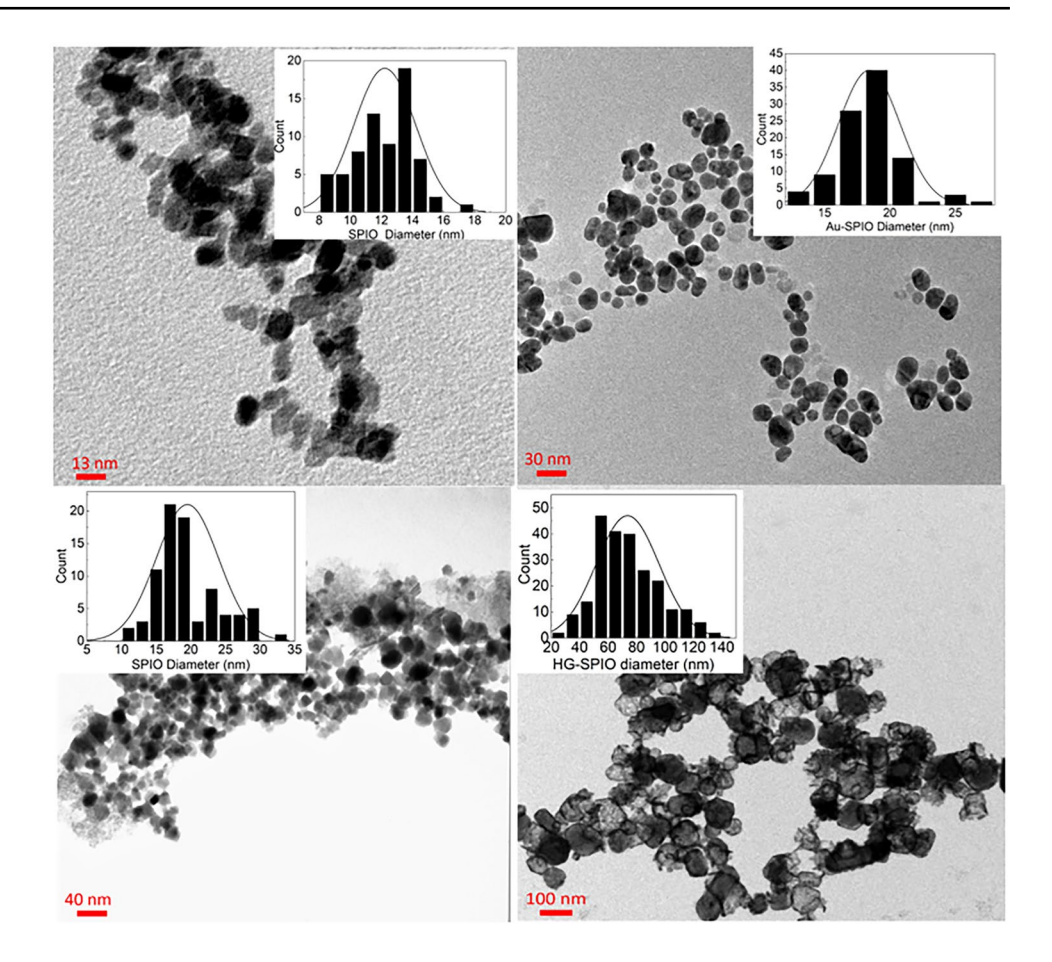


^bValue obtained from the literature [17]

^cValues were from the literature [41]

^dValues were from the equation [5-9]

Fig. 3 TEM images of a SPIO core in Au-SPIO NPs and b Au-SPIO NPs and c SPIO core of HG-SPIO NPs and d HG-SPIO NPs



where V_p is the volume of MPNPs and, χ_p and χ_f are the susceptibility of the MPNP and the fluid, respectively, and $\mu_0 = 4\pi \times 10 - 7$ H/m is the permeability of the free space. H_a is the applied magnetic field strength. Based on the TEM images in Fig. 3, each Au-SPIO NP has one SPIO NP core, while each HG-SPIO NP has multiple SPIO NP cores. The diameter distribution of Au-SPIO and HG-SPIO NPs and their core SPIO are given in Fig. 3a–d. This is verified by our elemental mapping analysis with the energy-dispersive X-ray spectroscopy [7]. The average number of SPIO in each HG-SPIO is calculated as

$$N = \frac{V_{core}}{V_{spio}} = \frac{\frac{4}{3}\pi d_{HG_{-}IN}^{3}}{\frac{4}{3}\pi d_{spio}^{3}} = \frac{d_{HG_{-}IN}^{3}}{d_{spio}^{3}}$$
(11)

where $d_{\text{HG_IN}}$ is the average inner diameter of HG-SPIO NPs, and d_{spio} is the average diameter of SPIO NP cores. The magnetic force provided by MF acted on each SPIO NP core is given by:

$$F_{\rm m}^{\rm A} = \mu_{\rm f} \left(N^* m_p \cdot \nabla \right) H_a \tag{12}$$

where μ_f is the permeability of the fluid. The magnetic force acted on each MPNP is given by:

$$F_{\rm m}^{\rm H} = \mu_{\rm f} (m_p \cdot \nabla) H_a \tag{13}$$

The opposing Stokes drag force on a spherical particle is given by

$$\overrightarrow{F_s} = 6\pi \eta R_H \overrightarrow{V_R} \tag{14}$$

When the Stokes drag force first equals the applied MF force, the particle will reach its equilibrium relative velocity, defined as,

$$\overrightarrow{V_R} = N^* \frac{\alpha^3}{9\eta R_H} \frac{\mu_0 \chi}{l + \frac{\chi}{3}} \nabla \left(\left| \overrightarrow{H} \right|^2 \right) = k \nabla \left(\left| \overrightarrow{H} \right|^2 \right)$$
(15)

where $k = \frac{a^3}{9\eta R_H} \frac{\mu_0 \chi}{1 + \frac{\chi}{3}}$ is the magnetic drift coefficient. Thus, considering these effects together, the concentration of MPNPs in the cerebral blood is given by:

$$\frac{\partial}{\partial t}C(x,y,t) = -\nabla \left[-D_{Total}\nabla C + \overrightarrow{CV_B} + Ck\nabla \left(\left| \overrightarrow{H}(x,y) \right|^2 \right) \right]$$
(16)



Here C is the concentration of MPNPs, $\overrightarrow{V_B}$ is the blood velocity.

Functionalized Au-SPIO and HG-SPIO NPs in the surrounding endothelial and tissue layer only experience diffusion and magnetic drift but no blood flow forces. The concentration inside the membrane and tissue is defined more simply by the equation:

$$\frac{\partial}{\partial t}C(x,y,t) = \nabla \left[-D_{\frac{endo}{tissue}} \nabla C + Ck \nabla \left(\left| \overrightarrow{H}(x,y) \right|^2 \right) \right]$$
(17)

After solving the equations, the permeability coefficient of the brain was calculated as [40]:

$$PAC_{BR} = \frac{dS}{dt} \times \frac{l}{A \times \Delta C \times v}$$
 (18)

Here, dS/dt is the amount of MPNPs passing the membrane in unit time, A is the surface area of the capillaries, ΔC is the average concentration difference between the cerebral blood and brain tissue, and v is the average blood velocity. The permeability coefficients of MPNPs for the brain without and with MF were further incorporated into the previously described PBPK model to estimate the amount of MPNPs staying in the brain tissue for every systemic circulation.

3.2.2 Other tissues' permeability identification

Based on reference [42], permeability for the liver and spleen was calculated by the equation:

$$PAC_{liver} = 0.0001336 \times d - 0.0016558.$$
 (19)

$$PAC_{spleed} = 0.0001448 \times d - 0.0004824.$$
 (20)

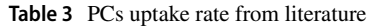
The biliary excretion rate is calculated as follows:

$$K_{bile} = 0.0005768^* ln \ ln(d) - 0.001449 \tag{21}$$

Here *d* is the MPNP's outer diameter.

3.3 Estimation of the PC uptake rate

PCs capture MPNPs from the tissue (for smaller MPNPs) or blood (for larger MPNPs), releasing part of them back into the tissue. The PC uptake rate is a function of the maximum uptake rate and decreases as the PCs reach a saturation level. The effective uptake rate by PCs is a function of a maximum uptake rate. The effective uptake rate decreases as the PCs become saturated. The experimental data [43] and curve fitting results [42] suggested that the uptake capacity, uptake, and release rate are related to MPNPs' size. Additionally, the cellular-uptake efficiency is affected by the size, morphology, surface-functionalization type, and surface coating of MPNPs [15]. Thus, we measured the uptake rate of



Reference	Diameter (nm)	Number of Au NPs per cell (10 ³)
[44]	22	290
[44]	39	120
[44]	66	74
[43]	14	300
[43]	50	60
[45]	74	41
[45]	100	20

two types of MPNPs and curve-fitted them with MATLAB. Simulation results using different approaches were compared. PCs' endocytosis of MPNPs is shown in the following equations:

$$K_{up} = K_{max} \times \left(1 - \frac{A_{pc}}{M_{PC_{Cap}} \times N_{PC}}\right)$$
 (22)

Here, $K_{\rm max}(h^{-1})$ is the maximum uptake rate in the tissue or blood, $A_{\rm pc}$ stands for MPNPs in PCs, $M_{PC\,\rm cap}$ is the uptake capacity per PC, $N_{PC,t}$ is the number of PCs in the different tissues. According to Curve fitting results [42], K_{max} and $M_{PC\,\rm cap}$ can be described as:

$$K_{\text{max}-t} = \text{UP}_{t} \times \left(\text{UP}_{t-1} \times \left(\text{d} - \text{UP}_{t_{-2}}\right)^{2} + \text{UP}_{t_{-3}}\right)$$
 (23)

$$M_{\text{PC cap}} = M_t \times \left(M_{t-1} \times \left(d - M_{L_{-2}} \right)^2 + M_{L_{-3}} \right)$$
 (24)

Here, UP_t and R_{ret_t} (unitless) are the coefficient for different tissues, and D_t, UP_{t1}, UP_{t2}, UP_{t3}, M_t , M_{t_11} , M_{t_22} , M_{t3} , D_t (unitless) are parameters (constants) calculated from available data by the literature [43, 44]. The collected PC uptake data is presented in Table 3.

Based on curve-fitting data, the obtained PK parameters for MPNPs are summarized in Table 4.

4 Results and discussion

4.1 MPNP characteristics

Figure 3 shows the morphology and the calculated diameters/historiography of (a) the SPIO core in Au-SPIO NPs (b) Au-SPIO NPs, (c) the SPIO core in HG-SPIO NPs, and (d) HG-SPIO NPs. From the historiographic diagram, we can calculate the average diameter of the SPIO core in Au-SPIO, and HG-SPIO NPs, which are 9.71 ± 0.09 nm, and 19.50 ± 0.05 nm, respectively. The average outer diameters



Parameter	Symbol	MPNP	Liver	Spleen	Kidneys	Lungs	Brain	Rest
Tissue: plasma distribution coefficient	P ^t (unitless) ^a	Au-SPIO	0.08	0.15	0.15	0.15	0.0360	0.15
		HG-SPIO	1.5	3	0.15	0.15	0.0360	0.15
Permeability coefficient	PAC _t (unitless) ^b	Au-SPIO	0.001	0.001	0.001	0.001	1.32*10 ⁻⁴ (MF -); 3.41*10 ⁻⁴ (MF +)	0.000001
		HG-SPIO	0.008	0.0099	0.001	0.001	3.0*10 ⁻⁵ (MF-); 6.2*10 ⁻⁵ (MF+)	0.000001
Maximum PC uptake rate	$K_{\text{max}}(1/h)^{1a}$	Au-SPIO	4	10	0.1	1	NA	NA
		HG-SPIO	4	10	0.1	0.1	NA	NA
Time for reaching half maximum uptake	$K_{50t}(h)^{c}$	Au-SPIO	24	24	24	24	NA	NA
rate		HG-SPIO	24	24	24	24	NA	NA
Hill coefficient	$n_{\rm t}$ (unitless) ^c ; $n_{\rm t}$ (unitless) ^c	Au-SPIO	2	2	2	2	NA	NA
		HG-SPIO	2	2	2	2	NA	NA
Release rate PC constant	$K_{\text{release}}(1/h^1)$	Au-SPIO	0.001	0.003	0.01	0.003	NA	NA
		HG-SPIO	0.0075	0.003	0.01	0.005	NA	NA
Biliary/ urinary excretion rate constant	K_{bile} (L/h) or K_{urine} (L/h) ^b	Au-SPIO	0.0001	NA	$3*10^{-6}$	NA	NA	NA
		HG-SPIO	0.0012	NA	$1.2*10^{-4}$	NA	NA	NA

^{a, b, c} values are from the literature [17], [23], and [42], respectively

of the Au-SPIO and HG-SPIO NPs are 18.42 ± 0.23 nm and 73.65 ± 1.46 nm, respectively.

Table 5 shows the increase of hydrodynamic diameter and zeta potential of MPNPs after the conjugation with PEG and insulin, indicating the successful functionalization of PEG and insulin.

The magnetic properties of MPNPs were measured using a vibration sample magnetometer. As shown in Fig. 4, magnetization curves appear s-shaped under the applied MF, and the MPNPs exhibit typical superparamagnetic behavior. The saturated magnetization is 56.94 emu/g, 16.23 emu/g, and 7.11 emu/g, for SPIO, AuSPIO, and HG-SPIO NPs, respectively. This result agrees well with the literature that the magnetization saturation of SPIO decreases when coated with Au [46].

Table 5 Zeta potential and hydrodynamic measurement of Au-SPIO and HG-SPIO NPs

Particle type	Hydrodynamic diameter (nm)	Zeta-potential (mV)
Au – SPIO	23.6 ± 0.1	-42.3 ± 0.8
Au – SPIO – PEG	38.0 ± 0.15	-26.4 ± 0.2
Au – SPIO – PEG – insulin	38.4 ± 1.2	-17.0 ± 0.1
HG – SPIO	115.5 ± 2.1	-30.6 ± 1.7
HG-SPIO-PEG	122.7 ± 1.3	-30.7 ± 0.3
HG-SPIO-insulin	125.8 ± 0.6	-23.4 ± 1.0

4.2 In vitro evaluation

The morphological impacts of MPNPs on the N2A neuron cell line are investigated, and the results are shown in Fig. 5. It can be noticed from the images that after 3 days of incubation, there is no significant change in morphology for Au-SPIO NP-treated cells. For HG-SPIO NP-treated cells, more dead cells and a reduced extent of neuronal cell

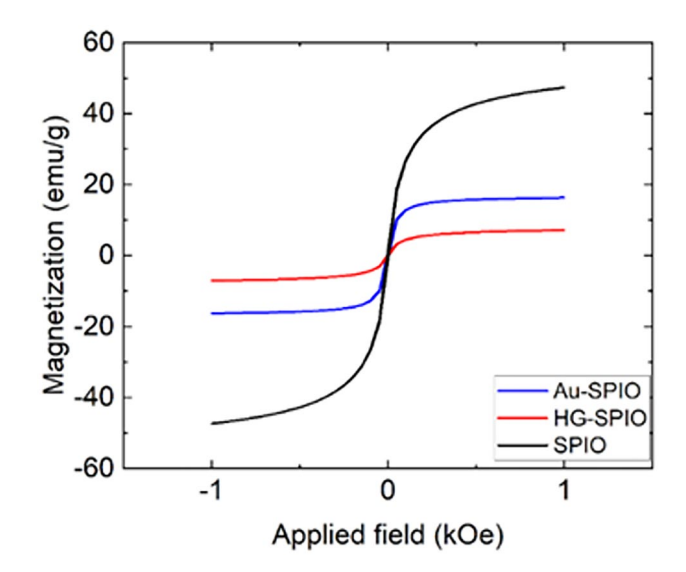
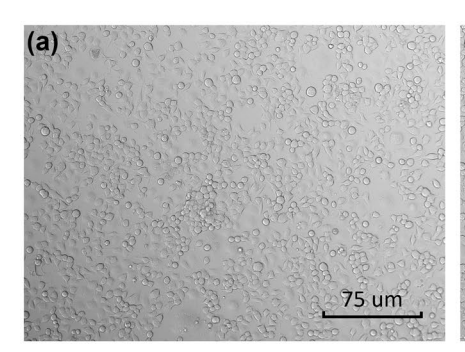


Fig. 4 Magnetization curves for SPIO NPs, Au-SPIO NPs, and HG-SPIO NPs $\,$







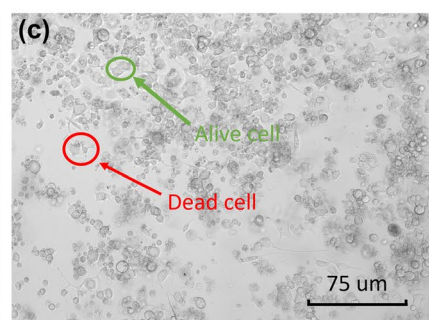


Fig. 5 Morphological changes in N2A cells. a Control, day 3, b Au-SPIO NPs at 40 μg/mL, day 3, and c HG-SPIO NPs at 40 μg/mL, day 3

differentiation are observed, indicating toxicity induced by HG-SPIO NPs at 40 µg/ml after 3 days of incubation.

The cell viability of Au-SPIO and HG-SPIO NPs was further evaluated on the N2A cell line using flow cytometry. As shown in Fig. 6, for up to 5 days of incubation, SPIO-Au NPs did not induce significant toxicity on N2A cells at 40 μ g/ml. For HG-SPIO NPs at the concentration of 20 μ g/ml, the cell viability was unaffected for up to 5 days of incubation. However, at a higher concentration (40 μ g/ml), there was reduced viability after 1 day of incubation. The overall viability of HG-SPIO NPs at 40 μ g/ml was lower than that at 20 μ g/ml and the viability of Au-SPIO NPs.

The results suggested that the larger size of NPs could induce higher toxicity. Therefore, a lower concentration of HG-SPIO NPs is favored for drug delivery to reduce the possible toxicity due to the high dose. The cell uptake rates of MPNPs at different time points were evaluated by quantifying the mass of Au in each sample using the ICP-MS. As shown in Table 6, the number of MPNPs absorbed by each cell was calculated based on the counted cell number in each well.

results that the cellular uptake rate reaches the maximum value at 4 h for both types of MPNPs. Additionally, at each time point, the cell uptake rate of Au-SPIO NPs is much higher than HG-SPIO NPs, indicating that the smaller size NPs are easier to be absorbed by cells.

4.3 Model prediction

The results are shown in Fig. 7 (a) and (b) for Au-SPIO

and HG-SPIO NPs respectively. It can be observed from the

For IP-injected MPNPs, MPNPs will first diffuse into the interstitial spaces of the portal organs and the lymph before entering the bloodstream. We applied an optimized bioavailability (F) to the dose based on our observation that a portion of the quantity remained trapped in the intraperitoneal space upon dissection. According to the reference that studied the biodistribution of IP-injected Au NPs [24], the optimized value of IP bioavailability is given as 76%. We simulated the biodistribution of IP-injected MPNPs (MF+and MF-) and compared them with measured biodistribution data. For Au-SPIO NPs, the blood, brain, liver, and lung prediction results show close to measured data (Fig. 8).

Fig. 6 MPNP-treated N2A cell viability for up to 5 days of incubation

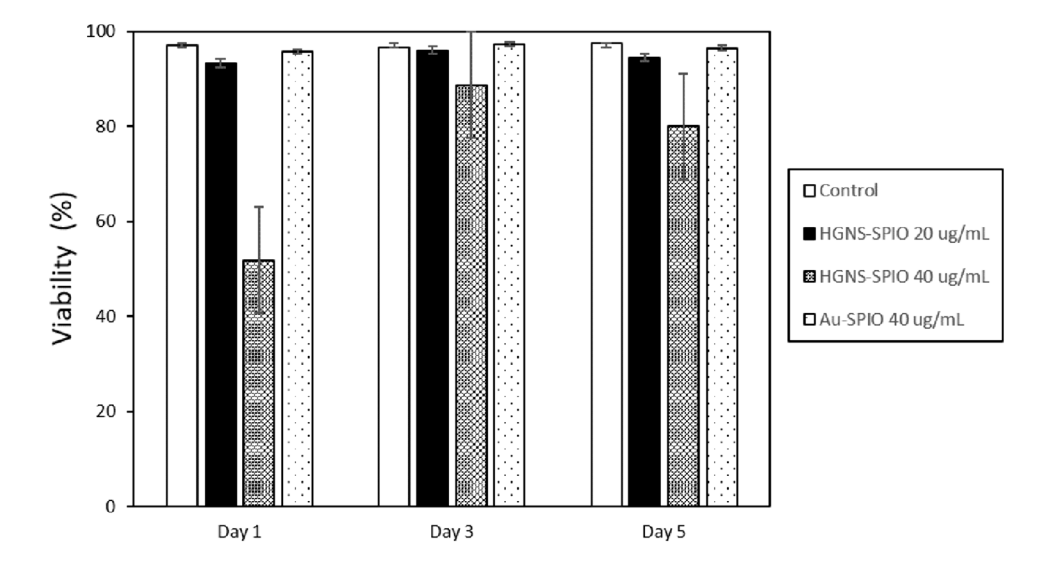




Table 6 Experimental N2A cellular uptake rate of Au-SPIO and HG-SPIO NPs

Time point	HG-SPIO (ng/10 ³ cell)	Au-SPIO (ng/10 ³ cell)
2 h	0.524	0.40
4 h	1.39	1.07
8 h	1.31	1.04
12 h	1.15	1.06

For HG-SPIO NPs, the prediction results for the liver and spleen are close to the measured data. At the same time, there is some deviation for blood and brain (Fig. 9). The difference in error bars' lengths is probably because of the large size of HG-SPIO NPs and the individual variability of the absorption rate in animals, as well as the small sample size. We will perform animal studies in a larger sample size in our future study to minimize the measurement variability. We discussed our evaluation methodology in the following section.

4.4 Model evaluation

The measured Au concentrations in blood, brain, liver, lung, kidney, and spleen were obtained at 2, 4, 8, and 12 h post IP injection of MPNPs at 30 mg/kg. The absolute average fold error (AAFE) was used to verify the PBPK model:

$$AAFE = 10^{\frac{1}{n}} \sum \left| log \left(\frac{simulated}{measured} \right) \right|$$
 (25)

Here n is the total number of data points. A larger AAFE value indicates a lower accuracy of prediction. The AAFE of model simulated data for each organ in each group is shown in Table 7. The AAFE of brain concentration for MF – groups is lower than for the MF + group for both types of MPNPs.

4.5 Model sensitivity analysis

We conducted normalized sensitivity analyses to identify highly influential parameters for optimal AAFE. We varied

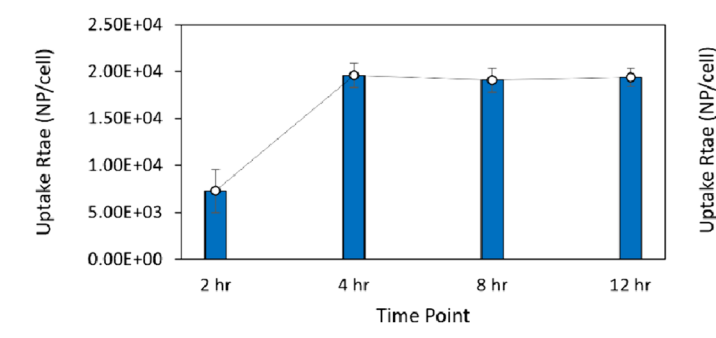


Fig. 7 N2A cellular uptake of a Au-SPIO NPs and b HG-SPIO NPs

each parameter by a 10% change of the initial value and calculated the area-under-the-concentration curve (AUC) in the plasma, liver, and spleen following:

$$S_{x}(\%) = \left(\frac{\text{AUC}_{\text{perturb}}}{\text{AUC}_{\text{base}}} - 1\right) \times 100\%$$
 (26)

As shown in Figs. 10a and 11a, the most sensitive PK parameters determining the brain accumulation of MPNPs are the PBR and Kbile for Au-SPIO NPs and PABRC and Kbile for HG-SPIO NPs. We will use these results for optimization in the discussion section.

4.6 Impact of MF

We investigated the effect of different MFs (MF-, MF+) on accumulating two types of MPNPs in the brain. The blood and three brain sections (midbrain, cortex, and cerebellum) were collected at 2, 4, 8, and 12 h after IP injection of MPNPs at 30 mg/kg, as shown in Figs. 12 and 13.

For the Au-SPIO NPs, the concentration of gold in the brain is 3.833 ng/ml for the MF – group and 3.608 ng/ml for the MF group. For the HG-SPIO NPs, the concentration of gold in the brain of the MF + group (0.854 ng/ml) is slightly higher than the MF – group (0.759 ng/ml), and the concentration in time points of 2 and 4 h are blank. The reason is that the accumulated concentration is too low to be detected within the ICP-MS test resolution. Note that the absolute value of gold accumulation in the brain also largely depends on the number of MPNPs entering the bloodstream upon injection. Sometimes, we can observe a noticeable amount of MPNPs accumulated in the injection site due to operating errors. Therefore, we normalized the brain concentration by the blood concentration.

Figure 14a shows that the MF+group has a higher gold level (normalized) at all time points than the MF-group, suggesting that the MF can enhance the BBB crossing of Au-SPIO NPs. As shown in Fig. 14b, the MF+group has a lower normalized gold level at 8 h and a slightly higher one at 12 h for HG-SPIO NPs. We did not observe the enhanced BBB crossing of HG-SPIO NPs by MF. According to our magnetization curve results

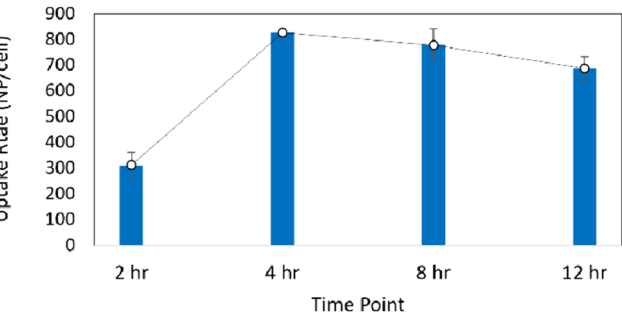
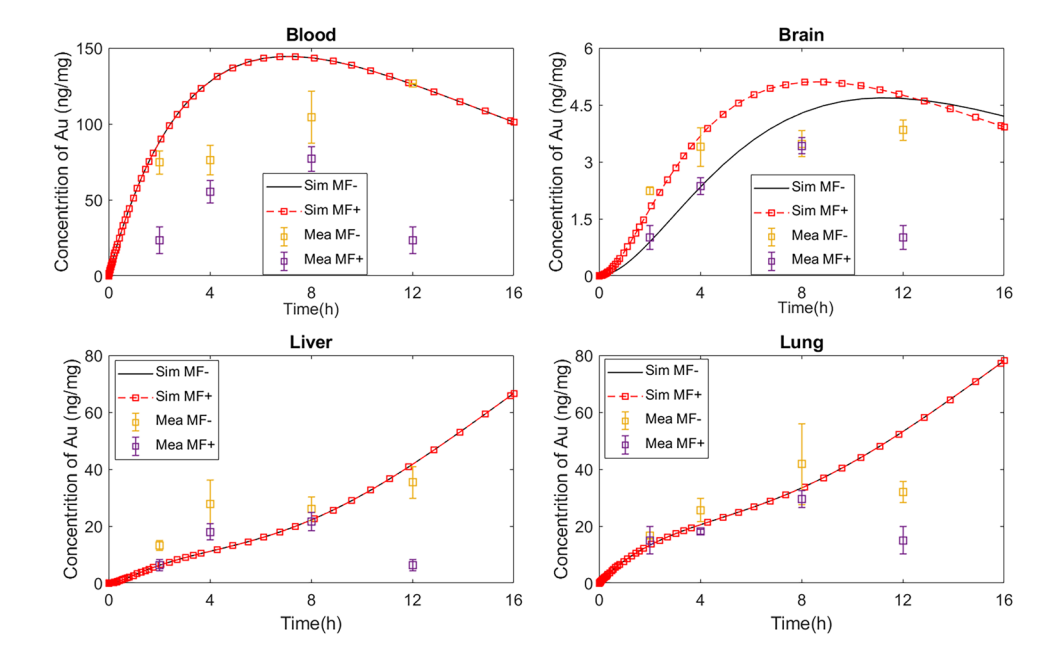




Fig. 8 Simulated and measured in vivo biodistribution of Au-SPIO NPs (MF – and MF +)



in Fig. 4, the thinner plasmonic layers of Au-SPIO NPs result in higher magnetization levels and thus significantly improve efficient BBB crossing exposure to the magnetic field. In contrast, there is no substantial improvement in BBB crossing efficiency for HG-SPIO NPs with increased shell thickness and less saturation magnetization. In brain tissues, most MPNPs are distributed in the cerebellum, fewer MPNPs are concentrated in the cortex, and the least amount is in the midbrain. We assume the MF has equal effects on the f MPNPs absorption in each area of the brain; the reason for the results may come from the mass difference samples; midbrain samples have the least mass, and the total amount of MPNPs in this area might be too limited for the ICP test to detect it. In other organs such as the spleen and livers, the MF has no effects on the biodistribution of MPNPs as the MF did not apply on these regions. The MF- and MF+ treatment groups show different results because

of the individual differences of each male mouse; the total number of MPNPs in each sample is a little different.

4.7 Impact of IP and IV injection types

As shown in Fig. 15a-b, the brain accumulation of gold post IP and IV injection of Au-SPIO NPs peaks at 12 and 8 h, respectively, while in Fig. 15c-d, the brain accumulation of gold post IP and IV injection of HG-SPIO NPs peaks at 8 h for both cases.

In addition, the brain concentration of gold in IP-injected MPNPs is higher than that of IV injection. In the *supplementary document*, Figure S1 presents the time history of blood concentration of gold of MPNPs after IP and IV injection. It shows that the gold concentration in blood decreases at 8 h. Additionally, As shown in Figs. S2

Fig. 9 Simulated and measured in vivo biodistribution HG-SPIO NPs (MF – and MF+)

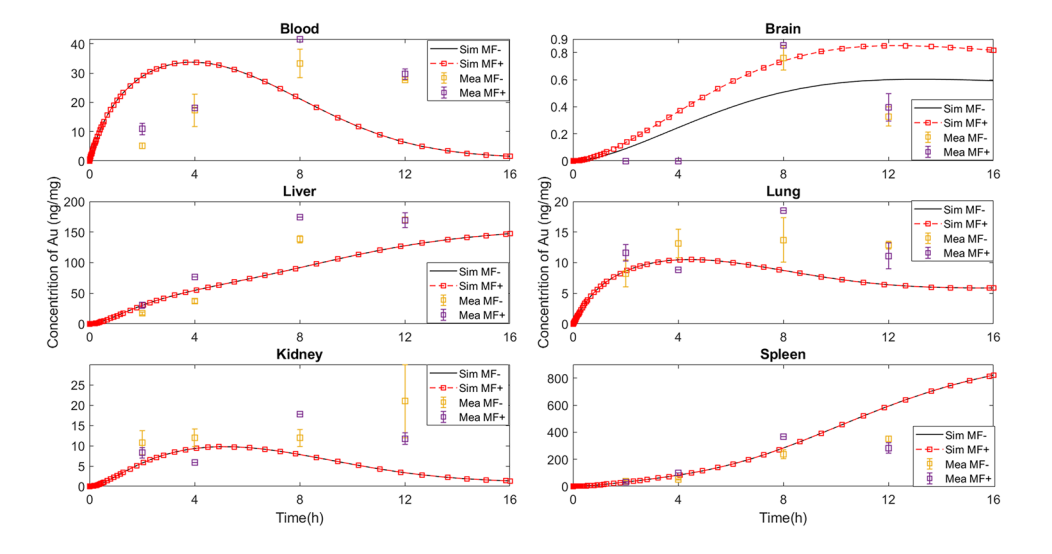




Table 7 AAFE of simulated biodistribution of MPNPs in different tissues

Tissue	Au-SPIO(MF-)	Au-SPIO(MF+)	HG-SPIO(MF-)	HG-SPIO(MF+)
Brain	1.5381	5.8266	1.1125	1.4213
Blood	1.8350	1.3600	1.3755	1.3501
Liver	2.4696	2.3732	1.1624	3.4275
Spleen	NA	NA	1.7818	1.2610
Kidney	NA	NA	5.7468	2.9385
Lung	1.0660	2.3074	2.1075	2.0656

and S3, for Au-SPIO NPs, the gold levels in the lungs and kidney by IV injection are higher than those by IP injection. But for the HG-SPIO NPs, the gold level in the liver, spleen, and kidney by IP injection is higher than that by IV injection. According to the literature, IV- and IP-injections can accumulate MPNPs in organs like the liver, spleen, and kidney [47]. However, literature suggested that the blood concentration of IP-injected Au NPs showed a slow increase followed by a steady state. In contrast, the blood concentration of IV-injected MPNPs decreased

biexponentially [33]. Therefore, there is always a vast and rapid decrease in gold levels in the blood after an IV injection compared to the relatively slow decline of gold levels after an IP injection. The reason is that IV-injected MPNPs directly enter the systemic circulation and rapidly reach a peak. Thus, MPNPs are distributed more quickly, and they are also cleared out more efficiently. Unlike IV injection, the IP-injected MPNPs undergo an absorption process by the peritoneal cavity before entering the systemic circulation. Therefore, the amount of gold in the

Fig. 10 PK parameter sensitivity analysis for Au-SPIO NPs in the **a** brain and **b** blood

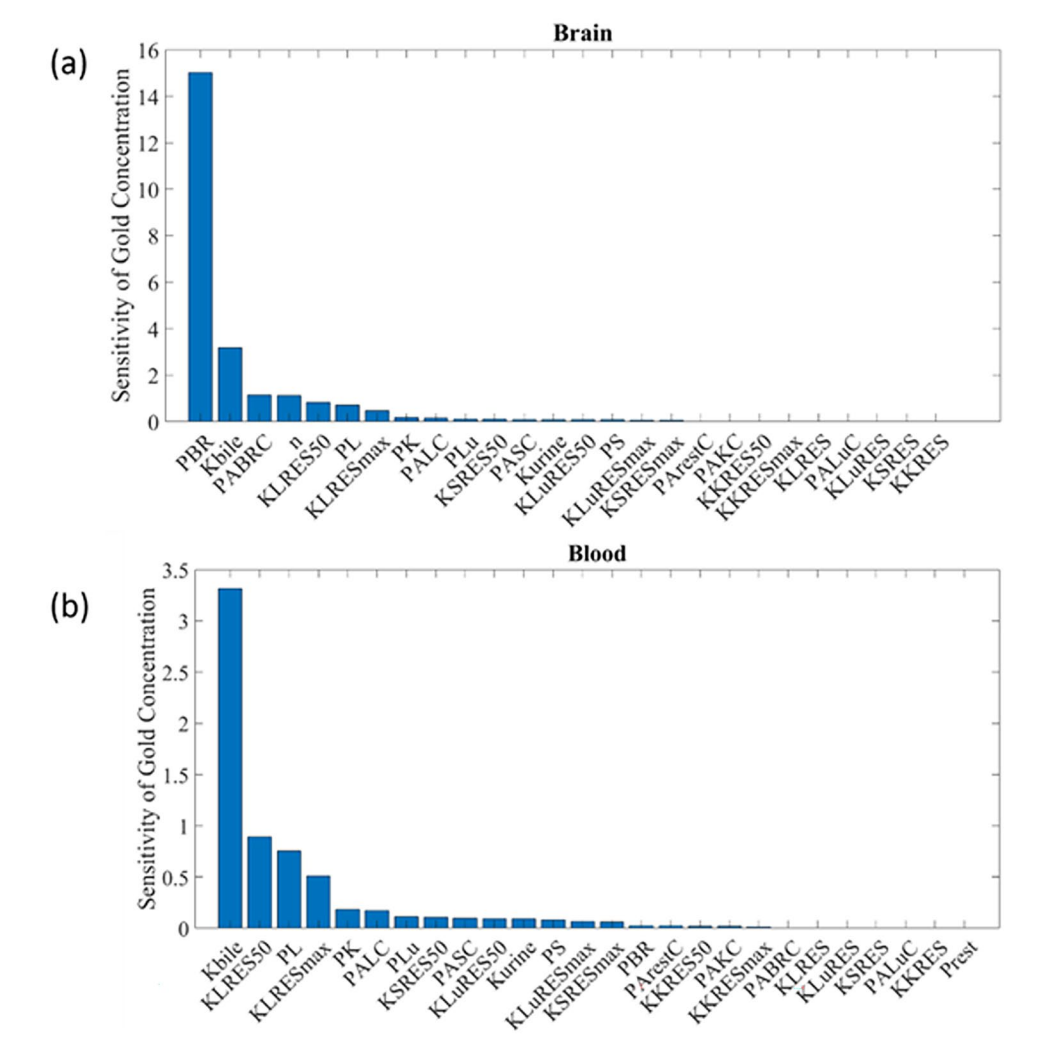
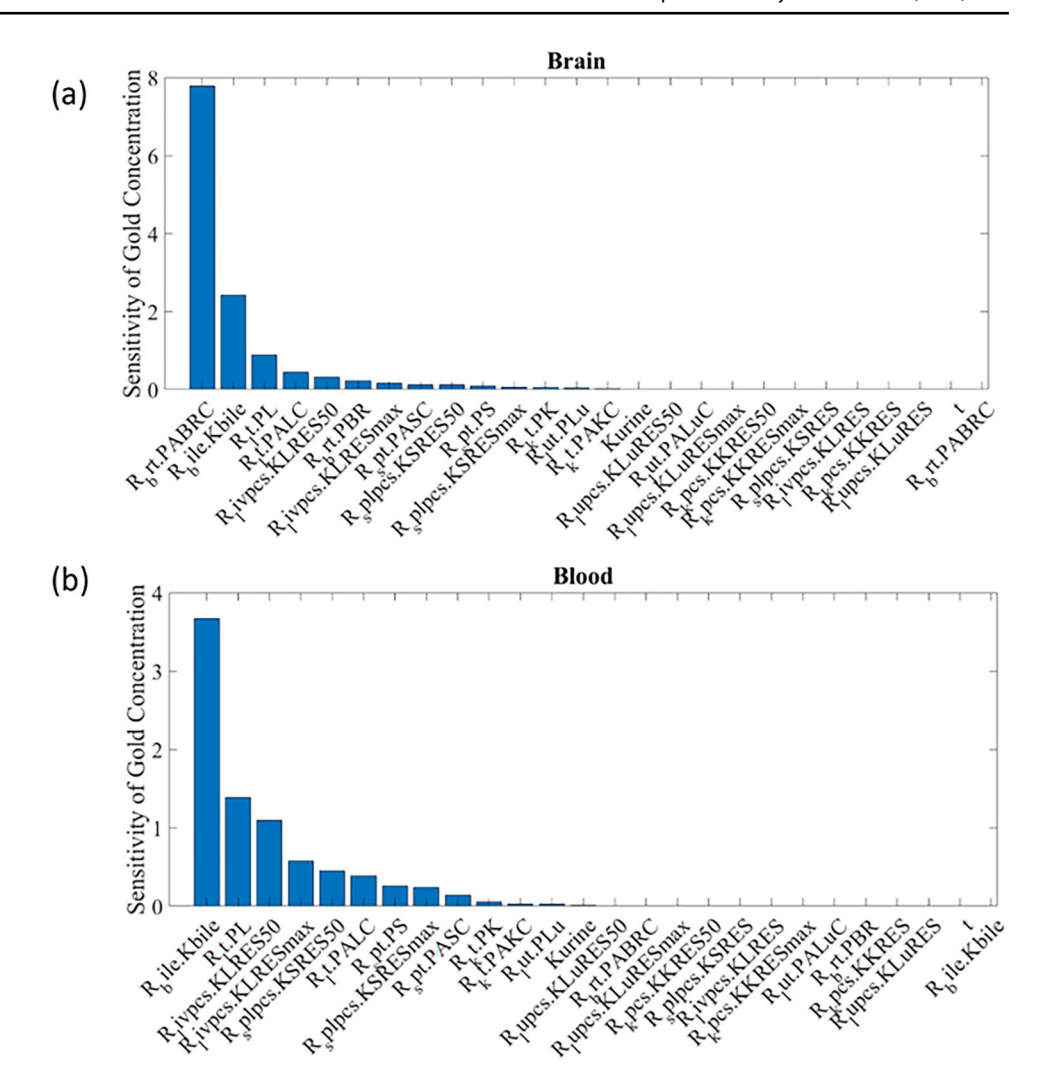




Fig. 11 PK parameter sensitivity analysis for HG-SPIO NPs in **a** brain and **b** blood



blood slowly increases after IP injection as MPNPs are constantly absorbed by the peritoneal cavity.

4.8 Impact of MPNP diameters

To investigate the impact of MPNP diameters on brain accumulation, we normalized the gold concentration in the brain by the gold concentration in the blood. We compared the non-normalized (Figs. 12d and 13d) and normalized (Fig. 14) results for both types of MPNPs. As we can see, both the non-normalized and normalized brain accumulation levels of Au-SPIO NPs are higher than those of HG-SPIO NPs, indicating that the smaller MPNPs can pass through BBB more efficiently. The size effect on brain gold accumulation is reported in the literature as well: Sonavane et al. [31] compared the biodistribution data of 4, 15, 28, and 58 nm Au NPs in mice and found that 15 nm Au NPs showed the highest concentration in the brain 24 h after IV injection, while on the contrary, as the particle

size increased, the concentration increased in the spleen. Betzer also found that 20 nm Au NPs showed the highest concentration levels in the blood for all time points from 2 to 48 h after IV injection compared to other sizes of Au NPs (50 nm and 100 nm), indicating the small size enhanced their BBB crossing efficiency and resulted in the highest brain accumulation over time [32]. Takeuchi pointed out that this difference in BBB crossing efficiency of colloidal Au NP at different sizes is because the surface area of the capillary basement membrane is covered by end-feet (button-like terminals of axons that make synaptic connections with other nerve cells) originating from brain astrocytes. These astrocytic end-feet are separated from the capillary endothelium by only 20 nm. Hence, Au NPs at smaller sizes may transfer through these gaps more quickly than their larger-size counterparts [48, 49].

Figure 16a-b shows that the concentration of HG-SPIO NPs is much higher than Au-SPIO NPs in the liver. Figure 16c shows that the HG-SPIO NP accumulation in the



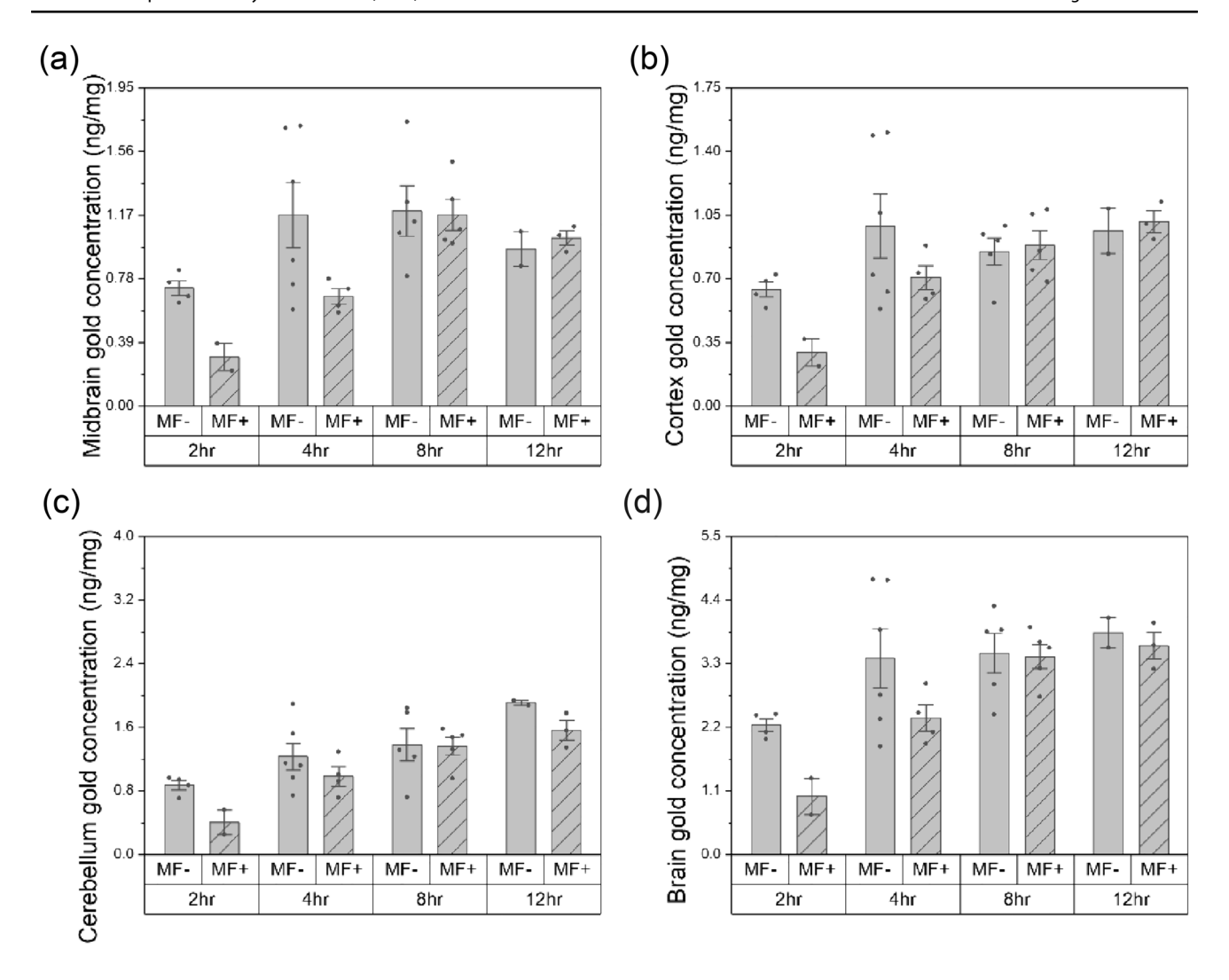


Fig. 12 Gold accumulation level in a midbrain, b cortex, c cerebellum, and d total brain at 2, 4, 8, and 12 h after IP injection of 30 mg/kg Au-SPIO NPs for MF-vs. MF+

spleen reaches 300 ng/mg after 12 h, the highest biodistribution among all tissues. According to a study of Au NPs from 10 to 100 nm diameter, the largest NP accumulations typically occur in the blood, liver, and spleen. Generally, larger nanoparticles accumulate in the liver and spleen more rapidly [50]. The study agrees well with our results that the high HG-SPIO NPs were measured in the liver and spleen. Organ biodistribution studies of Au NPs (15, 50, 100, and 200 nm) also showed that 15 nm Au NPs had a widespread concentration compared with larger sizes. An increase in spleen concentration was observed with the increase in particle size after 24 h of IV injection [31]. Literature also shows that the size of Au and Ag NP affects cellular uptake, biodistribution, and half-life [51]. For example, spherical mesoporous silica NPs with a 50 nm diameter showed the highest cellular uptake by HeLa cells at 10 min and 4 h after IV injection [52]. Au NPs coated with ethylene glycol (size from 10 to 100 nm) show NPs less than 50 nm protected by a moderate mPEG weight seem to have a long half-life and the ability to extravasate into and permeate through the tissue [53]. In addition, a study using targeted Au NPs reported the highest cellular uptake with 40-50 nm Au NPs in SKBR-3 cells [54]. These experimental studies provide empirical insights into designing MPNPs with optimal sizes, therapeutic effectiveness, and targeting efficiencies.

4.9 MPNP-related PK parameter optimization

The sensitivity analysis compares and selects sensitive biochemical-dependent PBPK parameters estimated by MATLAB optimization. Symbology supports a variety of



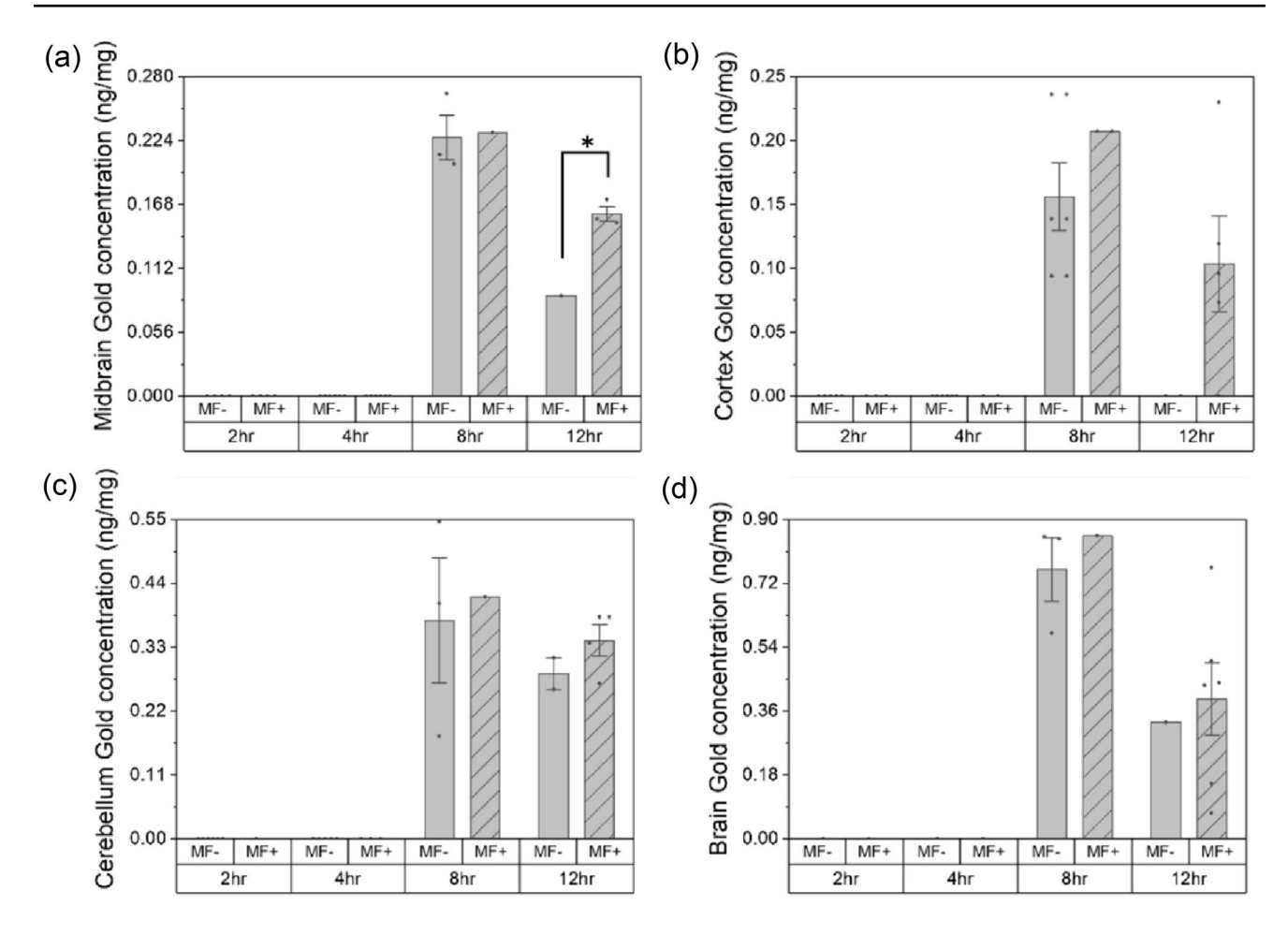


Fig. 13 Accumulation level of gold in a midbrain, b cortex, c cerebellum, and d brain at 2, 4, 8, and 12 h after IP injection of 30 mg/kg HG-SPIO NPs: MF-vs. MF+(*p<0.05)

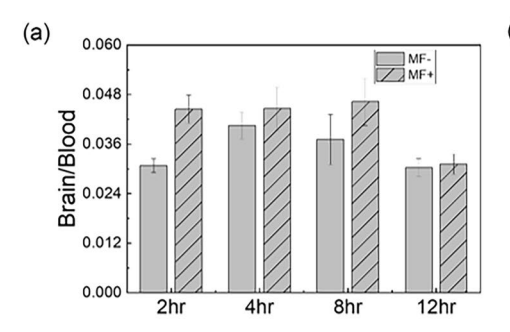
optimization methods for least-squares and mixed-effects estimation problems. Here, we introduced the nonlinear least square optimization toolbox [55] to evaluate the key parameters for brain concentration of MPNPs determined from our sensitive analysis. As discussed in Sect. 4.4, we chose the two most sensitive parameters (Kbile and PBR for Au-SPIO NP, Kbile and PABRC for HG-SPIO NP) for optimization. The optimized values for these parameters are listed in Table 8.

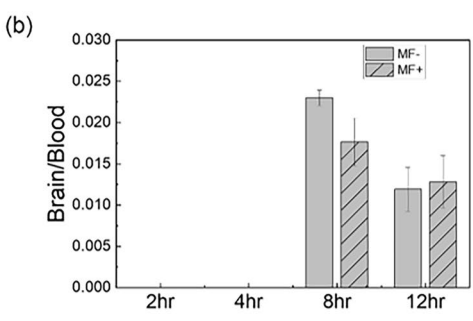
The optimized prediction of brain gold concentration is shown in Fig. 17. Compared with the simulated result

with original parameters, the simulated result with optimized parameters is closer to the measured data of brain gold concentration.

To further evaluate the accuracy of the simulated results using optimized parameters, we performed an AAFE evaluation. The results in Table 9 showed that the optimized predicting outcomes exhibited lower AAFE value compared with original results for MPNPs with and without MF, indicating that the optimized results are closer to measured data than the initial results.

Fig. 14 Normalized concentration level of gold in the brain by blood gold concentration for IP-injected MPNPs: a Au-SPIO NPs and bHG-SPIO NPs







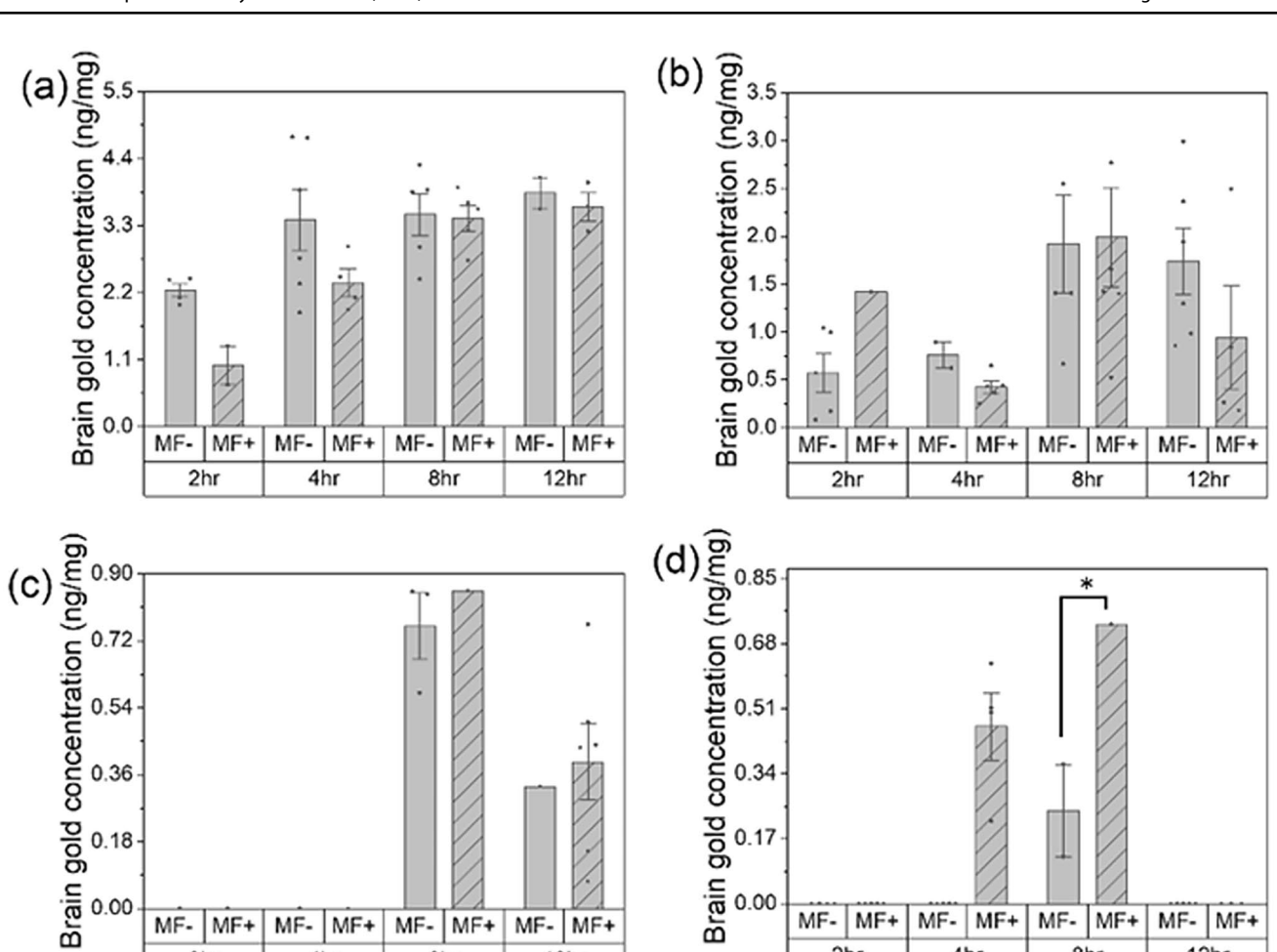


Fig. 15 Concentration level of gold in brain **a** Au-SPIO NPs through IP injection, **b** Au-SPIO NPs through IV injections, **c** HG-SPIO NPs through IP injection, and **d** HG-SPIO NPs through IV injections (*p<0.05)

12hr

However, due to the homogeneity and heterogeneity of NPs and animal models, developing a more comprehensive PBPK model still requires collecting much more diverse biological data from different animal species. Composing

4hr

8hr

2hr

a complete dataset to construct a robust PBPK model is virtually impossible. There are lots of factors which can affect PK parameters' estimation. For example, in the intrinsic factors (pregnancy, genetics, disease, organ dysfunction,

4hr

8hr

12hr

2hr

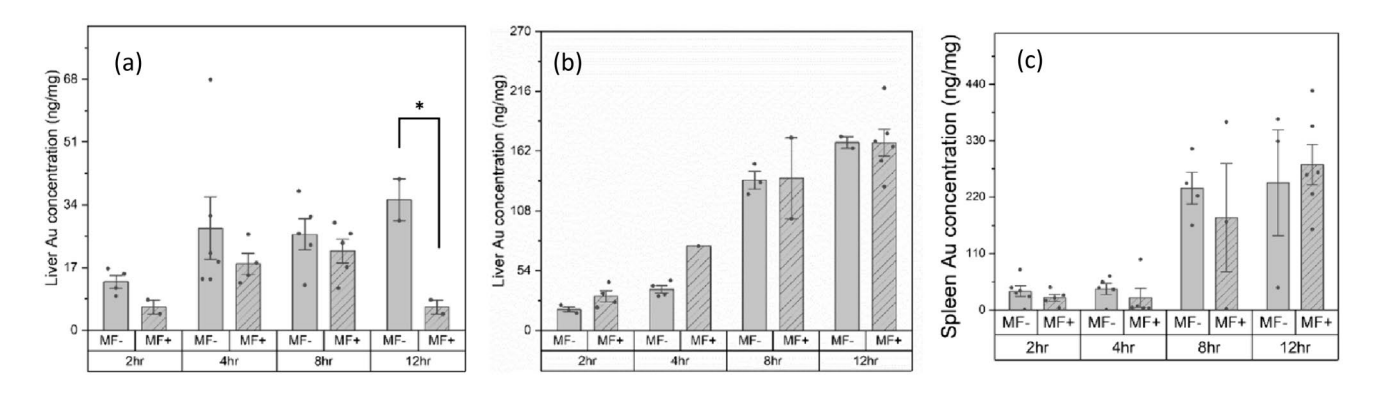


Fig. 16 Gold concentration of IP-injected a Au-SPIO NPs in the liver, b HG-SPIO NPs in the liver, and c HG-SPIO NPs in the spleen (*p<0.05)

Table 8 Optimized brain parameters

MPNPs	Biliary rate (Kbile)	Brain plasma distribution (PBR) for Au-SPIO NPs/brain permeability (PABRC) for HG-SPIO NPs
HG-SPIO NPs (MF –)	0.0334	3.0*10 ⁻⁵ (PABRC)
HG-SPIO NPs (MF+)	0.0212	6.2*10 ⁻⁵ (PABRC)
Au-SPIO NPs (MF –)	0.0016	0.0268 (PBR)
Au-SPIO NPs (MF+)	$6.59*10^{-4}$	0.0168 (PBR)

race) and extrinsic factors (diet, smoking, alcohol use, other medications) [56], in our model, we have not quantified these factors' influence on PK parameters. The use of machine learning (ML) and artificial intelligence (AI) approaches to predict the PK parameters is increasingly appealing because these novel approaches speed up the efficient development of robust PBPK models for drugs and NPs and have the potential to become an alternative approach to traditional in vivo-data-based PBPK modeling. For example, it always takes a long time to investigate and validate the permeability and drug development targeted to the central nervous system due to the extraordinary complexity of the brain. ML or AI algorithms are excellent for predicting BBB permeability with higher accuracy with limited data [57]. Compared with the in vivo and in vitro approach, which may involve complex physiological processes and hard-to-measure parameters accurately, ML/AI tools have significant advantages in prediction. However, the ML-based PBPK model still needs more interpretability for novel drugs. Integrating existing diffusion-limited and perfusion-limited approaches [21] and data processing techniques with experimental data is essential to help us better understand and predict the in vivo biodistribution of MPNPs and other NPs in general [58, 59]. In the future, the accuracy of the ML-PBPK model can be further improved or optimized for specific drug molecular structures by expanding the training set. We will keep updating our PBPK model to study the in vivo biodistribution of more types of MPNPs and apply AI approaches to estimate PK parameters accurately and efficiently.

5 Conclusion

This paper investigates the PBPK behavior of two types of MPNPs: functionalized Au-SPIO and HG-SPIO NPs with different sizes in the microvascular system. We developed a modern PBPK model that considers the impact of MPNP size on the brain plasma distribution coefficient and PC cellular uptake rate. We incorporate PB and PK parameters based on in vivo data from our experiments in adult mice and the literature. We validate our model using in vivo biodistribution of MPNPs in adult mice. The results showed that smaller-sized MPNPs have higher brain accumulation than larger sizes for both IP and IV injections. The full-body biodistribution results showed that most large MPNPs, like HG-SPIO NPs, enter the liver and spleen. In contrast, for smaller MPNPs like SPIO, Fe₃O₄ Au-SPIO, glycol-coated Au-SPIO NPs, and so on. The in vivo results also demonstrated that MF enhances the

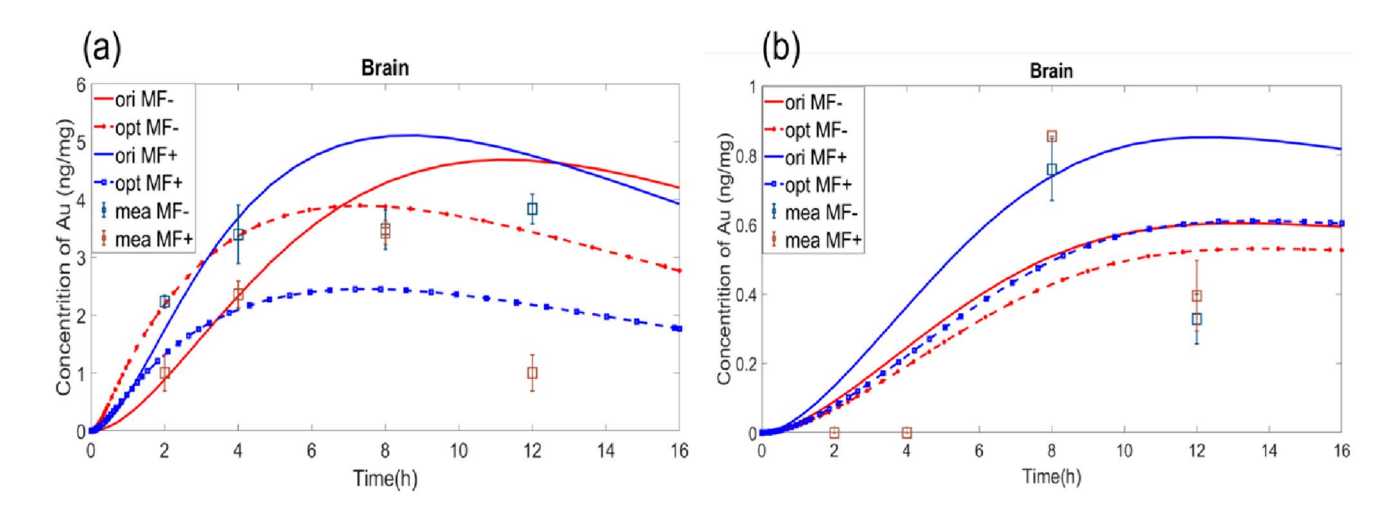


Fig. 17 Optimized (opt) and original(ori) simulation results compared with measurement (mea) results of brain concentration of gold in. a Au-SPIO NPs and b HG-SPIO NPs



Table 9 AAFE of Optimized results

MPNPs	Optimized results	Original results
Au-SPIO NPs (MF –)	0.1248	0.2777
Au-SPIO NPs (MF+)	0.5127	0.6072
HG-SPIO NPs (MF –)	0.1928	0.3351
HG-SPIO NPs (MF+)	0.8421	1.3255

brain accumulation of MPNPs for both injection types. IP injections resulted in a higher brain MPNP accumulation than IV injections. The local sensitive analysis showed that the brain plasma distribution, brain permeability, and distribution coefficients were highly influential parameters for brain accumulation of MPNPs.

Based on these findings, we optimized PB/PK parameters using nonlinear least square fitting to arrive at a more accurate prediction. We compared the biodistribution for different MPNPs and discussed intrinsic and extrinsic impact factors, such as MPNP morphologies, surface functions, and injection methods. The comparative study provides theoretical insight into designing MPNPs and biodegradable nano- [60, 61] and micro-scale [62] drug carriers. Much research has been done to investigate MPNP application as a functional filler in electromagnetic composites. Examples include MPNPs in electromagnetic composites such as Epsilon-negative cermet [63], doped ceramics [64], and C/SiO₂ meta-composite [65] to enhance further the development of therapeutic agents with multiple action modes. Applications also include bio-printed microrobots that can release smaller MPNPs continuously and sustainably [66] for brain-targeting drug delivery. In the next step, we will explore a more accurate friction and adhesion and the slippage model of microrobots into the PBPK model. We will develop an AI-empowered autonomous feedback control system to deliver the microrobots and nano drug carriers precisely to the targeted brain sites.

Supplementary Information The online version contains supplementary material available at https://doi.org/10.1007/s42114-024-00884-9.

Acknowledgements The authors thank the Material Characterization Facility and the Elemental Analysis Laboratory at Texas A&M University for their help.

Author contribution The manuscript was written through the contributions of all authors. Hanwen Hu, Muzhaozi Yuan, Jingfan Chen, Tianzhu Fan, and Tianhao Yan performed material preparation, characterization, and results analysis. In vitro cell work was performed by Nguyen Nguyen and Zhifeng Xiao. In vivo animal work was performed by Caitlin A Madison. Hanwen Hu and Muzhaozi Yuan prepared the initial draft of the manuscript. Ying Li, Shoshana Eitan, Hong-Cai Zhou, Jean-Philippe Pellois, and Ya Wang reviewed and revised previous manuscript versions. All authors have read and approved the final version of the manuscript.

Funding This work was kindly supported by the United States National Science Foundation (award # CMMI 1851635, Y.W.; award # ECCS 2021081, Y.W. and Y.L.). This work was also supported by the award

R01GM110137 (J.-P.P.) from the US National Institute of General Medical Sciences.

Availability of data and material The datasets generated and analyzed during the current work are available from the corresponding author upon reasonable request.

Declarations

Conflict of interest The authors declare no competing interests.

References

- Elmi GR et al (2022) Recent advances of magnetic gold hybrids and nanocomposites, and their potential biological applications. Magnetochemistry 8(4):38
- Dykman LA, Khlebtsov NG (2014) Uptake of engineered gold nanoparticles into mammalian cells. Chem Rev 114(2):1258–1288
- Wang X et al (2022) Fe3O4@PVP@DOX magnetic vortex hybrid nanostructures with magnetic-responsive heating and controlled drug delivery functions for precise medicine of cancers. Adv Compos Hybrid Mater 5(3):1786–1798
- Jia W et al (2021) Facile fabrication of monodisperse CoFe2O4 nanocrystals@dopamine@DOX hybrids for magnetic-responsive on-demand cancer theranostic applications. Adv Compos Hybrid Mater 4(4):989–1001
- Chowdhury P et al (2018) Chitosan biopolymer functionalized gold nanoparticles with controlled cytotoxicity and improved antifilarial efficacy. Adv Compos Hybrid Mater 1(3):577–590
- Yuan M, Wang Y, Qin YX (2017) SPIO-Au core–shell nanoparticles for promoting osteogenic differentiation of MC3T3-E1 cells: concentration-dependence study. J Biomed Mater Res, Part A 105(12):3350–3359
- Yuan M et al (2021) Superparamagnetic iron oxide—gold nanoparticles conjugated with porous coordination cages: towards controlled drug release for non-invasive neuroregeneration. Nanomed Nanotechnol Biol Med 35. p 102392
- Yuan M et al (2019) Thermocouple-tip-exposing temperature assessment technique for evaluating photothermal conversion efficiency of plasmonic nanoparticles at low laser power density. Rev Sci Instrum 90(9):094902
- Yuan M, Wang Y, Qin YX (2018) Promoting neuroregeneration by applying dynamic magnetic fields to a novel nanomedicine: superparamagnetic iron oxide (SPIO)-gold nanoparticles bounded with nerve growth factor (NGF). Nanomed Nanotechnol Biol Med 14(4):1337–1347
- Yuan M, Wang Y, Qin YX (2019) Engineered nanomedicine for neuroregeneration: light emitting diode-mediated superparamagnetic iron oxide-gold core-shell nanoparticles functionalized by nerve growth factor. Nanomed Nanotechnol Biol Med. p 102052
- 11. Yuan M et al (2022) Magnetic fields and magnetically stimulated gold-coated superparamagnetic iron oxide nanoparticles



- differentially modulate L-type voltage-gated calcium channel activity in midbrain neurons. Appl Nano Mater 5(1):205–215
- Reddy GR et al (2006) Vascular targeted nanoparticles for imaging and treatment of brain tumors. Clin Cancer Res 12(22):6677-6686
- 13. Al-Jamal KT et al (2016) Magnetic drug targeting: preclinical in vivo studies, mathematical modeling, and extrapolation to humans. Nano Lett 16(9):5652–5660
- Zhang J et al (2023) Nanoliposomal Bcl-xL proteolysis-targeting chimera enhances anti-cancer effects on cervical and breast cancer without on-target toxicities. Adv Compos Hybrid Mater 6(2):78
- Yuan M et al (2022) Progress, opportunities, and challenges of magneto-plasmonic nanoparticles under remote magnetic and light stimulation for brain-tissue and cellular regeneration. Nanomaterials 12(13):2242
- Yuan M et al (2022) Superparamagnetic iron oxide-enclosed hollow gold nanostructure with tunable surface plasmon resonances to promote near-infrared photothermal conversion. Adv Compos Hybrid Mater. pp 1–12
- 17. Chen J et al (2022) Blood-brain barrier crossing using magnetic stimulated nanoparticles. J Control Release 345:557–571
- Kutumova EO et al (2022) Physiologically based pharmacokinetic modeling of nanoparticle biodistribution: a review of existing models, simulation software, and data analysis tools. Int J Mol Sci 23(20):12560 %@ 1422-0067
- Qian MR et al (2017) Diffusion-limited PBPK model for predicting pulmonary pharmacokinetics of florfenicol in pig. J Vet Pharmacol Ther 40(6):e30–e38
- Utembe W et al (2020) Current approaches and techniques in physiologically based pharmacokinetic (PBPK) modelling of nanomaterials. Nanomaterials 10(7):1267
- Li M et al (2017) Physiologically based pharmacokinetic (pbpk) modeling of pharmaceutical nanoparticles. AAPS J 19(1):26–42
- Li M et al (2010) Physiologically based pharmacokinetic modeling of nanoparticles. ACS Nano 4(11):6303–6317
- Lin Z, Monteiro-Riviere NA, Riviere JE (2016) A physiologically based pharmacokinetic model for polyethylene glycol-coated gold nanoparticles of different sizes in adult mice. Nanotoxicology 10(2):162–172
- 24. Aborig M et al (2019) Biodistribution and physiologically-based pharmacokinetic modeling of gold nanoparticles in mice with interspecies extrapolation. Pharmaceutics 11(4):179
- 25. Chou W-C et al (2022) Development of a multi-route physiologically based pharmacokinetic (PBPK) model for nanomaterials: a comparison between a traditional versus a new route-specific approach using gold nanoparticles in rats. Part Fibre Toxicol 19(1):1–19 %@ 1743-8977
- Dubaj T et al (2022) Pharmacokinetics of PEGylated gold nanoparticles: in vitro—in vivo correlation. Nanomaterials 12(3):511
- LePage KT et al (2005) On the use of neuro-2a neuroblastoma cells versus intact neurons in primary culture for neurotoxicity studies. Crit Rev Neurobiol 17(1):27–50
- 28. Yang L et al (2017) Comparisons of the biodistribution and toxicological examinations after repeated intravenous administration of silver and gold nanoparticles in mice. Sci Rep 7(1):3303
- Daems N et al (2020) In Vivo Pharmacokinetics, biodistribution and toxicity of antibody-conjugated gold nanoparticles in healthy mice. J Biomed Nanotechnol 16(6):985–996
- Lasagna-Reeves C et al (2010) Bioaccumulation and toxicity of gold nanoparticles after repeated administration in mice. Biochem Biophys Res Commun 393(4):649–655
- Sonavane G, Tomoda K, Makino K (2008) Biodistribution of colloidal gold nanoparticles after intravenous administration: effect of particle size. Colloids Surf B Biointerfaces 66(2):274–280

- 32. Betzer O et al (2017) The effect of nanoparticle size on the ability to cross the blood-brain barrier: an in vivo study. Nanomedicine (Lond) 12(13):1533–1546
- Jung C et al (2014) Intraperitoneal injection improves the uptake of nanoparticle-labeled high-density lipoprotein to atherosclerotic plaques compared with intravenous injection. Circ Cardiovasc Imaging 7(2):303–311
- Al Shoyaib A, Archie SR, Karamyan VT (2019) Intraperitoneal route of drug administration: should it be used in experimental animal studies? Pharm Res 37(1):12
- Bachler G, von Goetz N, Hungerbühler K (2013) A physiologically based pharmacokinetic model for ionic silver and silver nanoparticles. Int J Nanomed 8:3365–3382
- Li D et al (2014) Physiologically based pharmacokinetic modeling of polyethylene glycol-coated polyacrylamide nanoparticles in rats. Nanotoxicology 8(sup1):128–137
- Brown RP et al (1997) Physiological parameter values for physiologically based pharmacokinetic models. Toxicol Ind Health 13(4):407–484
- 38. Zarrinkoob L et al (2015) Blood flow distribution in cerebral arteries. J Cereb Blood Flow Metab 35(4):648-654
- Fournier RL (2017) Basic transport phenomena in biomedical engineering. CRC Press
- Chen J, Wang Y (2020) Personalized dynamic transport of magnetic nanorobots inside the brain vasculature. Nanotechnology 31(49):495706
- Yankova G et al (2021) Cerebral arterial architectonics and CFD simulation in mice with type 1 diabetes mellitus of different duration. Sci Rep 11(1):3969
- Deng L et al (2019) Endocytosis mechanism in physiologicallybased pharmacokinetic modeling of nanoparticles. Toxicol Appl Pharmacol 384:114765
- Chithrani BD, Ghazani AA, Chan WCW (2006) Determining the size and shape dependence of gold nanoparticle uptake into mammalian cells. Nano Lett 6(4):662–668
- Chithrani BD, Chan WCW (2007) Elucidating the mechanism of cellular uptake and removal of protein-coated gold nanoparticles of different sizes and shapes. Nano Lett 7(6):1542–1550
- Nambara K et al (2016) Reverse size dependences of the cellular uptake of triangular and spherical gold nanoparticles. Langmuir 32(47):12559–12567
- Woodard LE et al (2018) Nanoparticle architecture preserves magnetic properties during coating to enable robust multi-modal functionality. Sci Rep 8(1):12706
- 47. Mitusova K et al (2022) Overcoming the blood–brain barrier for the therapy of malignant brain tumor: current status and prospects of drug delivery approaches. J Nanobiotechnol 20(1):412
- Takeuchi I, Onaka H, Makino K (2018) Biodistribution of colloidal gold nanoparticles after intravenous injection: effects of PEGylation at the same particle size. Bio-Med Mater Eng 29(2):205–215
- Olivier J-C (2005) Drug transport to brain with targeted nanoparticles. NeuroRx 2(1):108–119
- Dreaden EC et al (2012) Size matters: gold nanoparticles in targeted cancer drug delivery. Ther Deliv 3(4):457–478
- Hoshyar N et al (2016) The effect of nanoparticle size on in vivo pharmacokinetics and cellular interaction. Nanomedicine 11(6):673-692
- Lu F et al (2009) Size effect on cell uptake in well-suspended, uniform mesoporous silica nanoparticles. Small 5(12):1408–1413
- Perrault SD et al (2009) Mediating tumor targeting efficiency of nanoparticles through design. Nano Lett 9(5):1909–1915
- Jiang W et al (2008) Nanoparticle-mediated cellular response is size-dependent. Nat Nanotechnol 3(3):145–150



- 55. Shilo M et al (2015) The effect of nanoparticle size on the probability to cross the blood-brain barrier: an in-vitro endothelial cell model. J Nanobiotechnol 13(1):19
- 56. Reyner E et al (2020) Intrinsic and extrinsic pharmacokinetic variability of small molecule targeted cancer therapy. Clin Transl Sci 13(2):410-418
- 57. Singh AV et al (2021) Emerging application of nanorobotics and artificial intelligence to cross the BBB: advances in design, controlled maneuvering, and targeting of the barriers. ACS Chem Neurosci 12(11):1835-1853
- 58. Peer CJ, Chau CH, Figg WD (2017) Jumping the barrier: modeling drug penetration across the blood-brain barrier. Clin Cancer Res 23(24):7437-7439
- 59. Markicevic M et al (2021) Emerging imaging methods to study whole-brain function in rodent models. Transl Psychiatry
- 60. Qin L et al (2022) Resveratrol-silica aerogel nanodrug complex system enhances the treatment of sports osteoarthritis by activating SIRT-1. Advanced composites and hybrid materials 6(1):3
- 61. Wan J et al (2023) Novel strategy of senescence elimination via toxicity-exempted kinome perturbations by nanoliposome-based thermosensitive hydrogel for osteoarthritis therapy. Adv Compos Hybrid Mater 6(3):104
- 62. Bakadia B et al (2022) Biodegradable and injectable poly(vinyl alcohol) microspheres in silk sericin-based hydrogel for the

- controlled release of antimicrobials: application to deep fullthickness burn wound healing. Adv Compos Hybrid Mater 5(4):2847-2872
- 63. Fan G et al (2021) Dielectric dispersion of copper/rutile cermets: Dielectric resonance, relaxation, and plasma oscillation. Scripta Mater 190:1-6
- 64. Fan G et al (2021) Doped ceramics of indium oxides for negative permittivity materials in MHz-kHz frequency regions. J Mater Sci Technol 61:125-131
- 65. Xie P et al (2017) C/SiO2 meta-composite: overcoming the λ /a relationship limitation in metamaterials. Carbon 125:1-8
- 66. Chen J, Hu H, Wang Y (2023) Magnetic-driven 3D-printed biodegradable swimming microrobots. Smart Mater Struct 32(8):085014

Publisher's Note Springer Nature remains neutral with regard to jurisdictional claims in published maps and institutional affiliations.

Springer Nature or its licensor (e.g. a society or other partner) holds exclusive rights to this article under a publishing agreement with the author(s) or other rightsholder(s); author self-archiving of the accepted manuscript version of this article is solely governed by the terms of such publishing agreement and applicable law.

